2012

Effects Of Allotropic Transformations On Interdiffusion Behavior In Binary Systems

Ashley Elizabeth Ewh
University of Central Florida

EFFECTS OF ALLOTROPIC TRANSFORMATIONS ON INTERDIFFUSION BEHAVIOR IN BINARY SYSTEMS

by

ASHLEY ELIZABETH EWH
B.S. University of Central Florida, 2011

A thesis submitted in partial fulfillment of the requirements
for the degree of Master of Science in Materials Science and Engineering
in the Department of Mechanical, Materials and Aerospace Engineering
in the College of Engineering and Computer Science
at the University of Central Florida
Orlando, Florida

Summer Term
2012

Major Professor: Yongho Sohn

ABSTRACT

Diffusion plays a significant role in most materials systems by controlling microstructural development. Consequently, the overall properties of a material can be largely dependent upon diffusion. This study investigated the interdiffusion behavior of three binary systems, namely, Mo-Zr, Fe-Mo, and Fe-Zr. The main interest in these particular metals is for application in nuclear fuel assemblies. Nuclear fuel plates generally consist of two main components which are the fuel and the cladding. Due to diffusional interactions that can occur between these two components, a third is sometimes added between the fuel and cladding to serve as a diffusion barrier layer. Fe, Mo, and Zr can act as either cladding or barrier layer constituents and both Mo and Zr also serve as alloying additions in uranium based metallic fuels. Therefore, a fundamental understanding of the diffusional interactions in these systems is critical in predicting the performance and lifetime of these fuels.

In order to study this diffusion behavior, a series of solid-to-solid diffusion couples were assembled between Fe, Mo, and Zr. These couples were then diffusion annealed isothermally for various predetermined times over a range of temperatures, including some both above and below the allotropic transformation temperatures for Fe and Zr. Following the diffusion anneal, the couples were water quenched, cross-sectioned, and prepared for microstructural and compositional characterization. A combination of scanning electron microscopy (SEM), energy dispersive spectroscopy (EDS), and electron probe microanalysis (EPMA) were used to obtain micrographs showing the microstructure and to collect compositional data for identifying intermediate phases and determining concentration profiles across the interdiffusion zone.

Based on this characterization, the phases that developed in the diffusion zones were identified. In the Mo-Zr system, a large Zr solid solution layer developed in the couples annealed

at and above 850°C and a thin (~1-2 μm) layer of Mo_2Zr formed in all couples. Growth constants and concentration dependent interdiffusion coefficients were calculated for the Mo_2Zr and Zr solid solution phases, respectively. In the Fe-Mo system, both the λ-Fe_2Mo and μ-Fe_7Mo_6 phases were observed in couples annealed at 900°C and below while μ-Fe_7Mo_6 and α-Fe solid solution layers were observed in couples annealed above 900°C. The relevant growth constants and activation energies for growth were calculated. In the Fe-Zr system, the couple annealed at 750°C developed an $FeZr_2$ and an $FeZr_3$ layer while the couple annealed at 850°C developed an Fe_2Zr and $Fe_{23}Zr_6$ layer in the diffusion zone. The results of this analysis were then compared to available information from literature and the corresponding binary phase diagrams for each system. The results are discussed with respect to the effects of the allotropic transformations of Fe and Zr on the interdiffusion behavior in these systems.

The author would like to dedicate this work to her colleagues, friends, and family that have supported her throughout the years that have led up to this milestone.

ACKNOWLEDGMENTS

I would like to express my sincerest gratitude to my advisor, Dr. Yongho Sohn, for his continued support, guidance, and encouragement. My sincere appreciation also goes to my committee members Dr. Kevin Coffey and Dr. Challapalli Suryanarayana. I would also like to thank all of the faculty and staff of the department of Mechanical, Materials, and Aerospace Engineering (MMAE), the Advanced Materials Processing and Analysis Center (AMPAC), and the Materials Characterization Facility for their patience and assistance. Another thank you goes to all of my colleagues, especially Judith Dickson, in the Laboratory of Materials and Coatings for Extreme Environments (MCEE). Finally, I would like to acknowledge the Idaho National Laboratory, in particular Drs. Daniel Wachs, Bulent Sencer, Rory Kennedy, and especially Dr. Dennis Keiser Jr., for their continued technical and financial support.

TABLE OF CONTENTS

LIST OF FIGURES

LIST OF TABLES

LIST OF ACRONYMS/ABBREVIATIONS

BSE	Backscatter Electron Micrograph
C_i	Concentration of Component i
$\widetilde{D}_i$	Interdiffusion Coefficient of Component i
$\widetilde{D}_o$	Pre-exponential Factor for Diffusion
EDS	Energy Dispersive Spectroscopy
EPMA	Electron Probe Microanalysis
IDZ	Interdiffusion Zone
$\widetilde{\vec{J}}_i$	Interdiffusion Flux of Component i
k_p	Parabolic Growth Constant
k_o	Pre-exponential Factor for Growth
N_i	Mole Fraction of Component i
Q_d	Activation Energy for Diffusion
Q_k	Activation Energy for Growth
R	Molar Gas Constant
SEM	Scanning Electron Microscopy
T	Anneal Temperature
V_m	Molar Volume
x	Position
x_o	Matano Plane Posistion
Y	Layer Thickness
ZAF	Atomic Number, Absorption, and Fluorescence Correction Factor

CHAPTER 1: INTRODUCTION

For over 150 years, scientists have been studying the phenomenon of atomic migration or diffusion. The reason for this continued interest is the fact that diffusion plays a significant role in most materials systems by controlling microstructural evolution. Through influencing phase presence, size, and distribution, diffusion determines the overall properties of a material and therefore directly impacts the performance of that material. Consequently, a basic understanding of the diffusion behavior between the various components of any given system is essential in order to be able to predict and tailor the microstructure to optimize it for a particular application.

One such application where diffusion plays an important role is in nuclear fuel systems. While there are many different types of nuclear reactors, most nuclear fuel plates generally consist of two main components which are the fuel and the cladding. The fuel can be either ceramic or metallic and contains the fissionable material while the cladding is the structural component and serves the purpose of containment. Many of the metallic fuels currently in use are uranium-based alloys with the alloying additions often being molybdenum or zirconium. The cladding materials are often aluminum alloys or stainless steels.

With the increased temperature during fabrication or irradiation, solid-state diffusional interactions occur between these fuel and cladding components. Depending upon the phases that form in the reaction zone and the growth rate of these reaction products, this diffusional interaction could have detrimental effects during reactor operation. Often, the formation of intermetallics can cause excessive swelling and heat build up due to volume expansion and undesirable thermal properties which can in turn result in inefficient fuel performance, reduced service life of the fuel plates, or even catastrophic fuel failure. Another important component of nuclear fuels that can play a major role in the diffusion behavior of the system are the fission

products generated during irradiation including fission gas bubbles that form, which can add to the already drastic amount of swelling that occurs. Because this diffusional interaction takes place, a third component is sometimes added to the fuel system to function as a barrier layer between the fuel and cladding components and is intended to mitigate the reaction. Currently the most promising candidate materials for this diffusion barrier layer are molybdenum and zirconium.

The diffusion behavior in these systems can be quite complex due to the numerous components involved and largely determines the performance of the fuel. Understanding the behavior becomes complicated even further once irradiation effects are considered. Therefore, it is critical to simplify the studies to investigate binary diffusion involving the constituents used in nuclear fuels and then to systematically study the effects of each additional element. This particular work focused on analyzing the diffusion behavior in the Mo-Zr, Fe-Mo, and Fe-Zr systems via solid-to-solid diffusion couples to help further advance the knowledge of how these elements can affect the microstructural development in nuclear fuel systems.

The main objectives of this work were to identify the phases that form in the reaction zones of diffusion couples between Mo and Zr, Fe and Mo, and Fe and Zr, to calculate any relevant kinetic data such as growth constants and interdiffusion coefficients, and to investigate the effects of the allotropic transformations of Fe and Zr on both the phase formation and growth kinetics. While the initial motivation of this work was for applications in nuclear fuel systems, the observations and data obtained from this study can be useful for other applications as well. The phase constituent information and kinetic data calculated based on the diffusion couples examined in this study could be implemented into experiments and simulations regarding any other systems containing these components.

CHAPTER 2: LITERATURE REVIEW

2.1 Diffusion

2.1.1 Definition and Driving Force

The phenomenon of diffusion refers to the process by which atoms, ions, or molecules migrate in a gas, liquid, or solid. More specifically, solid-state diffusion refers to atomic transport in solid phases. Many chemical and microstructural changes in solids take place as a result of diffusion. Several processes that effect the evolution of a material, including precipitation, oxidation, and creep, are diffusion controlled processes. Therefore, analyzing this movement of atoms allows for an understanding of the microstructure and consequently the properties of a material.

Any process that requires a change in local chemistry occurs via diffusion [1]. In crystalline solids this means that individual atoms must exchange positions on the crystal lattice. This solid-state diffusion takes place due to the presence of defects in the material [2]. The existence of vacancies and interstitial atoms are responsible for lattice diffusion. However, diffusion can also occur along line and surface defects such as grain boundaries, dislocations, and free surfaces. Diffusion is generally more rapid along these larger defects than in the lattice through point defects so they are typically referred to as high diffusivity or short circuit diffusivity paths. The rate at which this exchange occurs can be different for each atomic species and varies as a function of composition and temperature [1].

The overall driving force for diffusion to occur is to lower the free energy of the system in order to reach the lowest possible energy state or equilibrium. Several different factors can contribute to this driving force including a chemical potential gradient, an electrical potential

gradient, a thermal gradient, or a stress gradient. In this work, only a chemical potential gradient was imposed during an isothermal diffusion anneal in the form of a concentration gradient created by placing two pure metals in contact. If these two metals are in contact at a sufficiently high temperature, interdiffusion will occur [3]. In other words, the atoms will migrate in order to reduce the imposed concentration gradient thereby reducing the free energy of the system.

2.1.2 Gibbs Phase Rule

Depending upon the nature of the two pure metals and the annealing temperature and time, the elements will have a different concentration distribution. If the two starting metals are completely miscible at the anneal temperature, the resulting concentration profile will be relatively smooth with no discontinuities [3]. However, if the two starting metals are only partially miscible or react to form intermediate phases, discontinuities will appear in the concentration profiles that are closely related to the binary phase diagram of the system [3]. Examples of the two situations are shown in Figure 1 for reference. While the exact profile within each phase cannot be determined based on the phase diagram, the concentration values at any interfaces can be obtained from the phase diagram assuming equilibrium conditions [3]. The reason for the formation of the straight interface between α and β in the hypothetical A vs. B binary multiphase diffusion couple as shown in Figure 1d is that the couple must follow the basic thermodynamic consideration of the Gibbs phase rule. It follows that only single-phase regions can form in such a couple where temperature and pressure are fixed because an additional degree of freedom would be necessary in order to vary concentration or in other words for diffusion to occur. Therefore, two-phase regions and non-planar interfaces cannot develop during isothermal anneal of a binary diffusion couple.

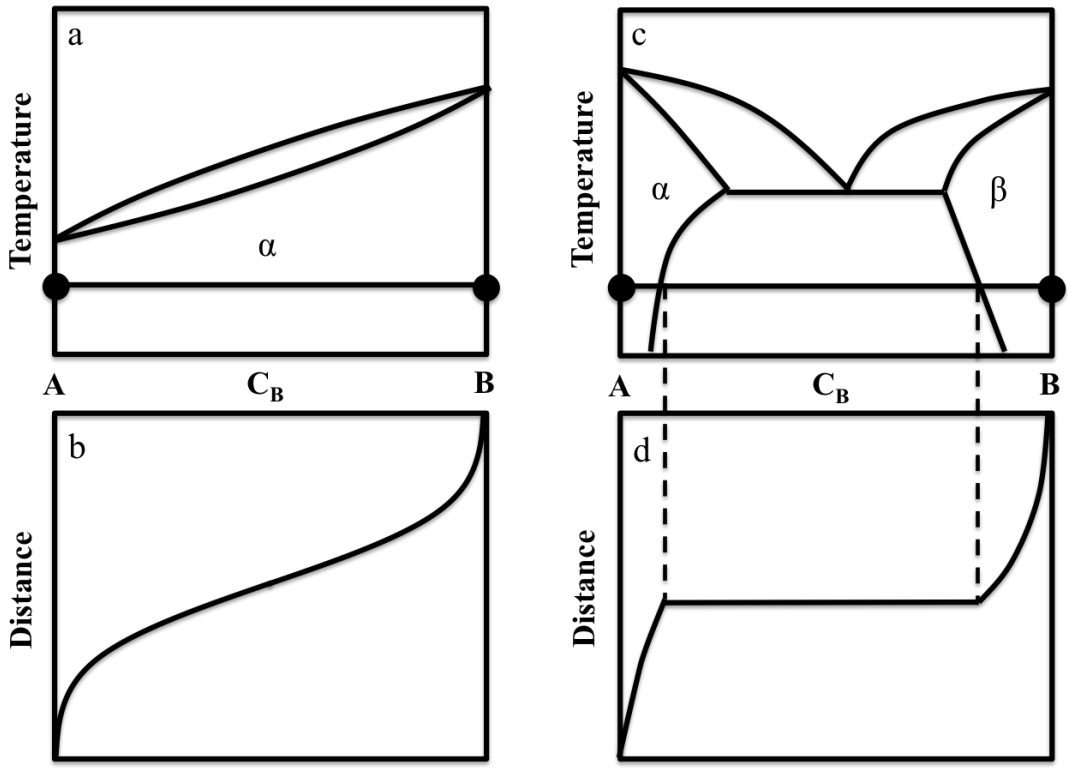

Figure 1: Schematics of a) isomorphous phase diagram of hypothetical A-B system b) corresponding concentration profile of an A vs. B diffusion couple annealed at the temperature indicated by the horizontal line c) eutectic phase diagram of hypothetical A-B system and d) corresponding concentration profile of an A vs. B diffusion couple annealed at the temperature indicated by the horizontal line.

2.1.3 Reaction Diffusion

Reaction diffusion is a process governed by both the rate of diffusion across the product phases and the reactions taking place at the interfaces [4]. Therefore, the growth kinetics of a compound layer are determined by a combination of both of the following processes [5]:

(i) the diffusion of matter across the compound layer where the diffusion flux slows down with increasing layer thickness

(ii) the rearrangement of atoms at the interfaces required for the growth of the compound layer.

In order for a compound layer to form, the diffusion of the reacting species is a necessary, but not sufficient step because, in addition, the chemical reaction step must follow the diffusion of the reactants for the formation of the product phase to occur [6]. More specifically, according to Dybkov, the process leading to an increase in thickness of a compound layer can be divided into two groups. The first group includes the steps that the duration of which are dependent on both the existing layer thickness and the increase in its thickness [6]. In this group, the only step involved is the diffusion of atoms within the compound layer or "internal" diffusion. The second group includes steps that the duration of which depends only on the increase in layer thickness. These steps include [6]:

(i) the transition of a given kind of atom from one phase into an adjacent one or "external" diffusion

(ii) the redistribution of atomic orbitals of the reacting elements, and

(iii) the rearrangement of the lattice of an initial phase into the lattice of a chemical compound.

A schematic of a hypothetical binary phase diagram where one compound layer exists between mutually insoluble elementary substances A and B is presented in Figure 2 to illustrate the growth process of the chemical compound A_pB_q [7]. The growth rate of the intermetallic A_pB_q is dependent on both the rate of B and A diffusing to the A/A_pB_q and A_pB_q/B interfaces, respectively, and the rate of the chemical reactions taking place at those interfaces. There are therefore typically two main growth regimes that describe compound layer formation. It follows that if the interfacial reaction controls the process, the kinetic description is called interface or reaction controlled [5]. In the initial stages of intermediate phase formation, the layer is still

relatively thin and thus provides a short diffusion path for the A and B atoms to migrate across the interface. This initial stage is typically reaction controlled since there is an essentially constant supply of atoms to the respective interfaces and is hence governed by the rate at which the atoms can arrange themselves into the lattice of the reaction product. In this case, the layer thickness increases linearly as a function of the anneal time. However, if the diffusion process is the rate-limiting factor and controls the growth rate, the corresponding kinetic description is termed diffusion controlled [5]. As the layer grows in thickness, it becomes increasingly difficult for the atoms to diffuse to the opposite interfaces to supply the reaction. Hence there are fewer atoms available to participate in the reaction in turn slowing down the reaction rate. For diffusion controlled processes, the layer thickness increases proportionally to the square root of the anneal time.

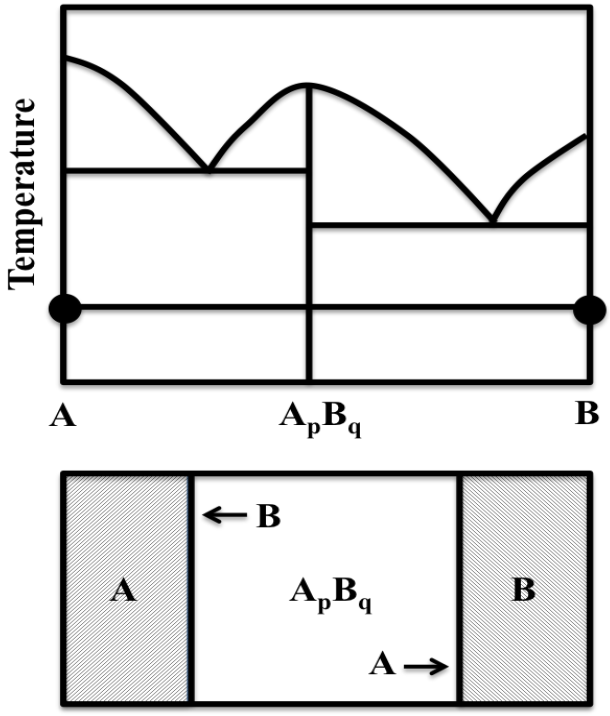

Figure 2: Schematic phase diagram to illustrate the growth process of the A_pB_q chemical compound layer at the interface between mutually insoluble elementary substances A and B.

When researchers initially considered reaction diffusion between two primary solid solutions, it was assumed that each phase present in the equilibrium phase diagram at the diffusion anneal temperature would form in the diffusion zone [8]. However, based on more recent research, not all of the stable intermediate compounds will necessarily grow to an observable thickness even after long anneal times [9]. Several investigations have been conducted to provide theoretical analyses of the formation and growth rates of intermetallic compound layers in binary systems [8-12]. According to these studies, there are several factors that influence the growth rate of a compound layer. A particular intermediate phase will grow more rapidly if:

(i) the diffusion coefficient in the layer is larger

(ii) the diffusion coefficients in the surrounding phases are smaller

(iii) the homogeneity range of the phase is larger

(iv) the concentration range of the surrounding two-phase areas is narrower

(v) the crystal structures between adjoining phases are similar.

These observations, however, are not absolute. In fact, a phase may only obey one or two of these "rules" and still grow thicker than another. Therefore, further studies need to be conducted to more fully investigate the conditions under which intermetallic layers form and grow more rapidly.

2.1.4 Diffusion Equations

In order to understand the diffusion process, it is first necessary to be able to describe it using a formalism that relates how the atoms move to the current condition of the system. There are two main approaches to developing this description which are the atomistic approach and the

continuum approach. The atomistic approach describes the periodic jumping of individual atoms from one lattice site to another through statistical thermodynamics. The continuum approach assumes a continuum solid and does not assume a particular diffusion mechanism. The phenomenological expressions of irreversible thermodynamics are used in the continuum approach; hence, it is also sometimes referred to as the phenomenological approach. The continuum approach can be used to analyze and predict microstructural and composition evolution in a material. For the purposes of this study, the phenomenological approach was used for quantitative analysis of the diffusion couples.

The phenomenological formalism defines fluxes as measures of motion and relates them to forces defined in terms of gradients of the properties of the system calculated from the current condition of the system [1]. For example, it is a well known phenomenon that heat flows from hot to cold regions. Such a flux of heat in the presence of a temperature gradient is described by Fourier's Law as

$$J_q = -\kappa \frac{dT}{dx} \tag{1}$$

where J_q is the heat flux, i.e. the flow of heat per unit area of the plane through which the heat traverses per second, $\frac{dT}{dx}$ is the temperature gradient, and κ is the thermal conductivity. Here the minus sign reflects the fact that the heat flows from high to low temperatures; in the direction of heat flow the temperature gradient is $-\frac{dT}{dx}$.

Similarly, the phenomenological formalism, which yields Fick's Laws for diffusion in single-phase multicomponent systems, is widely accepted as the basis for the mathematical

description of diffusion [1]. The expression for the flow of particles from high concentration to low concentration is analogous to that for the flow of heat from hot to cold and is given by the expression

$$J_i = -D_i \frac{dC_i}{dx} \tag{2}$$

where J_i is the flux of component i, $\frac{dC_i}{dx}$ is the concentration gradient of component i, and D_i is the proportionality constant known as the diffusion coefficient of component i [2]. Again, the minus sign reflects the fact that the particles typically flow from regions of high concentration to low concentration. This relation is known as Fick's First Law and was named after Adolf Fick who first formulated it [13]. The flux represents the number of particles crossing a unit area per unit time. This concept is illustrated in Figure 3. In SI units, the concentration is expressed in terms of number of particles or moles per m^3 and the distance x in m. Therefore, the diffusion coefficient has units of m^2/s.

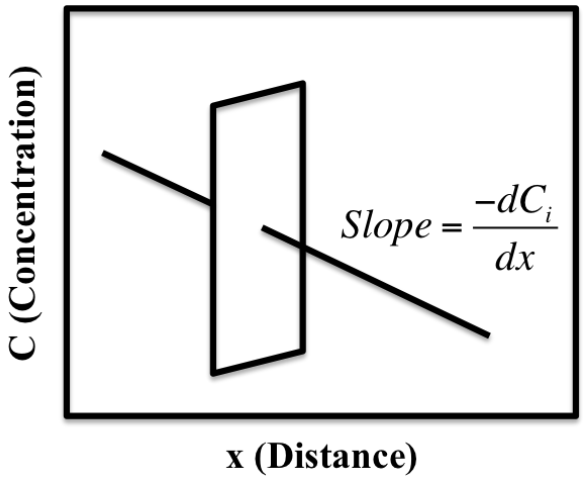

Figure 3: Schematic representation of Fick's First Law where the concentration gradient is the driving force for diffusion to occur.

Fick's First Law is applicable under steady state when there is no change in composition over time or, in other words, when $\frac{dC_i}{dt} = 0$ and the solution is relatively trivial. However, if the concentration varies as a function of time, the equation must be modified to account for the non-steady state or transient condition. If the concentration is changing over time, it means that the amount of material that entered the volume over a unit of time is different than that which left during that same time. In this case, the continuity equation, which represents the net increase in the concentration in the volume can be invoked and is expressed as

$$-\left(\frac{\partial J_i}{\partial x}\right) = \left(\frac{\partial C_i}{\partial t}\right) \tag{3}$$

The continuity equation can then be combined with Fick's First Law to obtain the expression

$$\left(\frac{\partial C_i}{\partial t}\right) = \frac{\partial}{\partial x}\left(D_i \frac{\partial C_i}{\partial x}\right) \tag{4}$$

If the diffusivity can be assumed to be constant, i.e. independent of concentration, this equation simplifies to a linear second order partial differential equation expressed as

$$\frac{\partial C_i}{\partial t} = D_i \frac{\partial^2 C_i}{\partial x^2} \tag{5}$$

This expression is known as Fick's Second Law and can provide an approximation of the concentration profile as a function of distance in the form of an error function solution if the

initial and boundary conditions are known and substituted into the equation [14]. This is an adequate solution for diffusion in systems in which the two starting metals are completely miscible at the anneal temperature like the hypothetical A-B system shown previously in Figure 1a. However, such a system is not typical in practice and the diffusion coefficient is generally a function of both concentration and temperature. This means that Equation 4 remains a nonlinear second order partial differential equation. Solutions to equations of this form cannot be obtained analytically and therefore must be found numerically.

When considering interdiffusion (or chemical diffusion) in binary systems, as observed with respect to a laboratory or fixed frame of reference, the diffusion coefficient is often a function of composition. The interdiffusion coefficient, denoted as $\widetilde{D}$, can be determined using a method known as the Boltzmann-Matano method [15, 16]. Based on Boltzmann's work, the nonlinear partial differential equation form of Fick's Second Law can be transformed into a nonlinear ordinary differential equation even when the interdiffusion coefficient is a function of concentration [15]. This is done by utilizing a scaling parameter, which is known as the Boltzmann parameter given by

$$\lambda = \frac{x}{\sqrt{t}} \tag{6}$$

where x is the distance and t is the time. Substituting Equation 6 into Equation 4 yields

$$-\frac{\lambda}{2}\left(\frac{\partial C_i}{\partial \lambda}\right) = \frac{\partial}{\partial \lambda}\left(\widetilde{D}_i \frac{\partial C_i}{\partial \lambda}\right) \tag{7}$$

Then, using this transformation, Matano developed a solution to the equation by considering the initial and boundary conditions for a binary diffusion couple of $C_i = C_L$ when $x < 0$ and $t = 0$ and $C_i = C_R$ when $x > 0$ and $t = 0$ [16]. This solution is expressed as

$$\widetilde{D}_i(C_i) = -\frac{1}{2}\frac{d\lambda}{dC_i}\int_0^{C_i} \lambda dC_i \tag{8}$$

under the condition that

$$\int_{C_L}^{C_R} \lambda dC_i = 0 \tag{9}$$

If the annealing time is constant, Equation 9 simplifies to

$$\widetilde{D}_i(C_i) = -\frac{1}{2t}\frac{dx}{dC_i}\int_{C_L}^{C} x dC_i \tag{10}$$

under the condition that

$$\int_{C_L}^{C_R} x dC_i = 0 \tag{11}$$

The location of the Matano plane, or the plane of mass balance, x_o, is determined when this condition is satisfied and is required for further analysis. The position of the Matano plane can be obtained from the experimental concentration profile and can then be used to calculate the

interdiffusion coefficient as described in further detail in section 3.3.2. This technique is valid as long as the semi-infinite boundary conditions are not violated meaning the concentrations at the terminal ends of the diffusion couple must remain unchanged. Also, the volume of the diffusion couple must be able to be assumed as a constant in order to use this method. For a binary system, this typically means that the total molar volume of the system must obey Vegard's Law, given as

$$V_m = V_A N_A + V_B N_B \tag{12}$$

where V_m is the total molar volume of the system, V_A and V_B are the partial molar volumes of components A and B respectively, and N_A and N_B are the mole fractions of components A and B respectively.

When interdiffusion, or diffusion with respect to a fixed reference frame, is considered certain constraints are imposed. These constraints are based on the conservation of mass and are given by

$$\sum_{i=1}^{n} \frac{\partial C_i}{\partial x} = 0 \quad \text{and} \quad \sum_{i=1}^{n} \widetilde{J_i} = 0 \quad (i = 1,2, \ldots n) \tag{13}$$

For a binary system, there are only two components and these constraints simplify to

$$\frac{\partial C_A}{\partial x} = -\frac{\partial C_B}{\partial x} \quad \text{and} \quad \widetilde{J_A} = -\widetilde{J_B} \quad (i = 1,2) \tag{14}$$

Therefore, $\widetilde{D_A} = \widetilde{D_B} = \widetilde{D}$ and there is only one interdiffusion coefficient for a binary system.

2.2 Allotropic Transformations

2.2.1 Phase Transformations

Most matter in the universe exists in three different states including solid, liquid, and gas. The stable phase of a material in the solid state is dependent on various thermodynamic properties including volume, pressure, and temperature. If any of these thermodynamic quantities is changed, the Gibbs free energy of the system will also change consequently. A phase transformation is said to occur if this change in free energy causes a change in the structure of the material. Such a phase transformation will only occur if the structure of the new phase will result in a lower free energy. The phase that has the minimum free energy under the particular set of thermodynamic conditions will be the equilibrium phase.

Phase transformations in materials can be characterized into two major modes which are homogeneous and heterogeneous transformations [17]. Homogeneous transformations occur over the entire volume of the material simultaneously while heterogeneous transformations occur in various regions over time. Further classifications of phase transformations can be made under these two main modes. Heterogeneous transformations involve a nucleation and growth process. This process occurs for both liquid-to-solid and some solid-to-solid transformations. Heterogeneous solid-to-solid transformations can also be divided into two main categories that involve thermally activated growth and athermal growth. The transformations that are thermally activated are called diffusional transformations. These diffusional transformations make up the majority of phase transformations that occur in the solid state and can be roughly divided into five different groups: (a) precipitation reactions, (b) eutectoid transformations, (c) order/disorder reactions, (d) massive transformations, and (e) polymorphic transformations [18]. Understanding

phase stability and phase transformations is essential in materials science because all of the properties of any material depend on its phase constituents. This section, however, will focus on the driving forces and examples of polymorphic transformations.

2.2.2 Polymorphic Transformations

Some materials exhibit more than one type of crystal structure depending primarily on temperature and sometimes on pressure, or severe deformation. Such a transformation of the crystalline structure without any change in the chemical composition can occur because one particular arrangement of atoms is more stable than another in certain temperature ranges [19]. The materials that exhibit this phenomenon are said to be polymorphic in nature. Polymorphism of pure metallic elements is called allotropism and more than 20 of the over 70 known metals have temperature allotropism [20]. Just a few of the materials that are known to exhibit this allotropic behavior are listed in Table 1 along with the crystal structures of the allotropes and the temperature ranges in which they are stable [21]. The important trend among these transformations is that, in most cases, the transformations are from a close-packed structure (hexagonal or fcc) at low temperatures to a more open structure (bcc) at high temperatures. For the purposes of this thesis, the allotropic transformations in Fe and Zr are of importance and will be discussed further. As shown in Table 1, there are two allotropes of Zr which are denoted as α-Zr and β-Zr. The low temperature allotrope is α-Zr and has an hcp crystal structure while the high temperature allotrope is β-Zr and has a bcc crystal structure. The transformation takes place at 863°C and follows the typical trend of transforming from a close packed structure at low temperature to a more open structure at high temperature. Fe, however, is an exception to this rule and hence will be described in more detail in section 2.2.4.

Table 1: Known allotropes of some materials.

Phase	Temperature Range (°C)	Crystal Structure	Pearson Symbol	Prototype
β-Be	1270 - 1289	bcc	cI2	W
α-Be	RT - 1270	hcp	hP2	Mg
α-Co	422 - 1495	fcc	cF4	Cu
ε-Co	RT - 422	hcp	hP2	Mg
δ-Fe	1394 - 1538	bcc	cI2	W
γ-Fe	911 - 1394	fcc	cF4	Cu
α-Fe	RT - 911	bcc	cI2	W
β-Gd	1235 - 1313	bcc	cI2	W
α-Gd	RT - 1235	hcp	hP2	Mg
β-Sn	13 - 232	tetragonal	tI4	Sn
α-Sn	< 13	diamond cubic	cF8	C
β-Ti	882 - 1670	bcc	cI2	W
α-Ti	RT - 882	hcp	hP2	Mg
γ-U	776 - 1135	bcc	cI2	W
β-U	668 - 776	tetragonal	tP30	U
α-U	RT - 668	orthorhombic	oS4	U
β-Y	1478 - 1522	bcc	cI2	W
α-Y	RT - 1478	hcp	hP2	Mg
β-Zr	863 - 1855	bcc	cI2	W
α-Zr	RT - 863	hcp	hP2	Mg

2.2.3 Driving Forces for Allotropic Transformations

As with any phase transformations, the driving force for an allotropic transformation to occur is the reduction of the Gibbs free energy of the system. In order for two different solid structures to be more stable at different temperatures the Gibbs free energy of the stable phase must be lower in that temperature range. Therefore, the existence of allotropism requires that the free energy curves for the two structures are intersecting [22]. This concept can be understood from the schematic free energy curves for a solid and liquid phase in Figure 4 [18]. Below the temperature of the intersection point of the two free energy curves, i.e. the melting point in this case, the solid phase is stable because it has the lower free energy in that temperature range. However, above the melting point, the liquid is the more stable phase and hence the transformation will occur at temperatures above that point. While this plot represents the change in free energy from the solid to liquid state, the same principle applies to an allotropic transformation. In order for an allotropic transformation to occur, there has to be a change in which phase has the lower free energy above a certain temperature. This means that the free energy curves of the two phases must intersect.

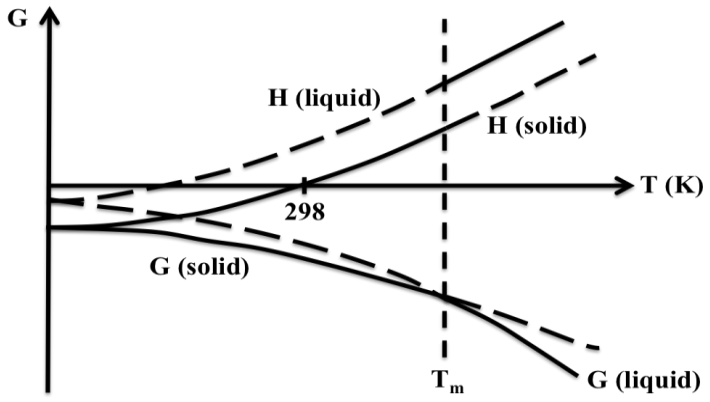

Figure 4: Variation of enthalpy (H) and free energy (G) with temperature for the solid and liquid phases of a pure metal.

The fact that the free energy curves must intersect indicates that the heat capacities of the two phases must be different. The value of the heat capacity is represented by the slope of the enthalpy curve as shown in Figure 5 [18]. The heat capacity can also be broken down into several components including the contributions from harmonic lattice vibration, anharmonic lattice vibration, electronic excitations, and magnetic excitations. Then the heat capacity is given as,

$$C_p = C_{ph} + C_{anh} + C_{el} + C_{magn} \tag{15}$$

where the terms in order denote the heat capacity from harmonic phonons, from anharmonicity in the lattice vibrations, from electronic excitations, and from magnetic excitations [22]. These factors, therefore, can all influence the final free energy of the different allotropes and might account for the fact that open structures are more stable at high temperatures while close-packed structures are more stable at low temperatures.

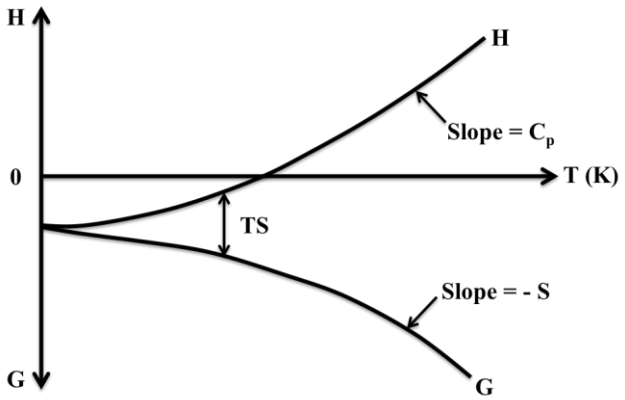

Figure 5: Variation of Gibbs free energy and enthalpy curves with temperature showing relation of C_p to slope of the enthalpy curve.

Two terms that can contribute to the overall heat capacity of the system are from the harmonic and anharmonic phonons that represent the modes of vibration in the crystal lattice. It has been argued by Zener that bcc structures are more favorable at high temperatures due to a more rapid decrease in free energy with temperature because a more open structure has a transverse phonon mode with a particularly low frequency [23]. This requires that there is a small structural dependence on the Debye temperature [22]. The Debye model treats lattice vibrations as phonons in a box and the Debye temperature represents the temperature at which the highest frequency mode and hence all modes of vibration are excited. Based on research conducted by Grimvall and Ebbsjo, there is a significant tendency for the free energy due to harmonic lattice vibrations (or equivalently the Debye temperature) of a bcc structure to be a few percent lower than that for fcc or hcp structures [22]. This agrees with Zener's assertion and suggests that this is one of the reasons that bcc is the more favorable high temperature structure. For simple metals the electrons are well described by a free electron gas and since the atomic volume is only changed by a few percent on allotropic transformations, there is no significant structure dependence on the free energy due to the electronic contribution for these metals. However, for transition metals, the d-band density of states can vary considerably with the lattice structure [24]. This may be a possible reason for allotropism in transition metals. Although the electronic free energy should be considered for transition metals like titanium and zirconium, the vibrational free energy contribution still plays a more significant role [24]. In many cases, the magnetic contribution to the free energy can be ignored. However, in cases like that of iron, it can play a significant role. For iron, it is necessary to consider the combined effect of the electronic and magnetic free energies in order to explain its allotropism. The allotropes of Fe will be discussed further in the following section.

2.2.4 Allotropes of Fe

As demonstrated by Table 1, there are many systems that exhibit allotropic transformations. Most of them follow a similar trend having a close-packed allotrope (hcp or fcc) at low temperature and a more open structure allotrope (bcc) at high temperature. Perhaps the most important industrially are the allotropes of iron. Pure iron has three different allotropes when considering atmospheric pressure. These include the α, γ, and δ phases. The α phase exists below 911°C and has a bcc crystal structure. Once it is heated above 911°C it changes to an fcc form called γ-Fe. This allotropic transformation plays a significant role in the heat treatment and processing of most steels so it is the more important transformation in this system. As γ-Fe is heated above 1392°C it changes once again back to a bcc lattice. This high temperature allotrope is known as the δ phase. Finally iron melts at 1536°C. These transformations and transformation temperatures are indicated on the schematic heating and cooling cycle shown in Figure 6 [19].

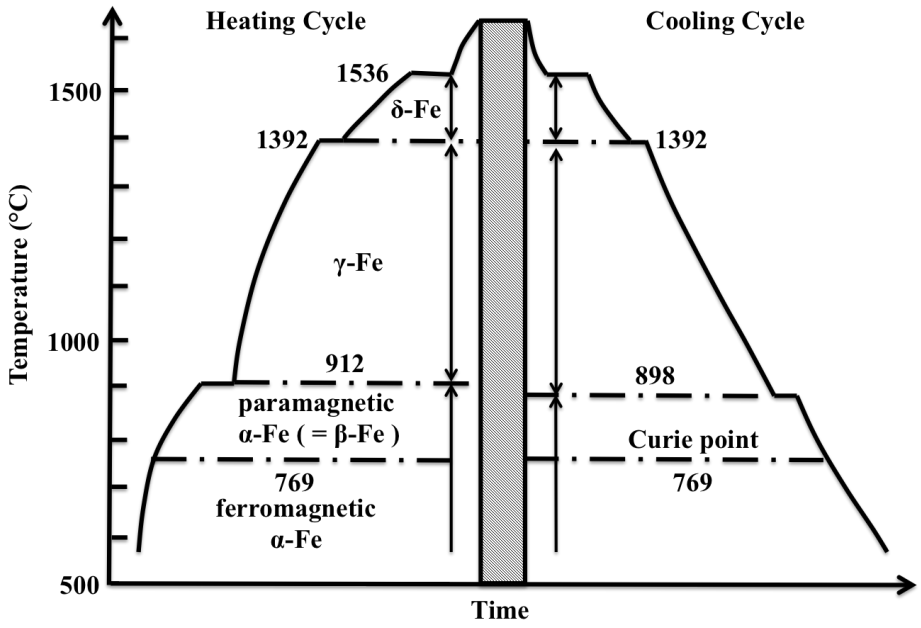

Figure 6: Allotropic transformations of iron during heating and cooling.

One of the reasons for its industrial importance is that the high temperature γ-Fe phase has a significantly higher solubility for carbon than the low temperature α phase. This fact is exploited in steel making and used in order to supersaturate α-Fe and then perform additional heat treatments to tailor the final microstructure and properties of the steels. In theory, the allotropic transformations in any case should occur at the same temperatures upon heating and cooling. However, this is not necessarily the case because of the necessity of undercooling. The transformations therefore take place at lower temperatures during cooling than upon heating as suggested in Figure 6 for the γ to α-Fe transformation. The difference between the allotropic transformation temperature upon heating and cooling is known as temperature hysteresis. As the cooling rate increases the temperature hysteresis also increases.

Iron is a unique case because, based on the typical trend, the lower temperature α-Fe phase should be close-packed i.e., hcp or fcc, and the higher temperature γ-Fe phase should be a more open structure like bcc. This trend is followed, however, in the γ to δ-Fe as γ-Fe is fcc and δ-Fe is bcc. The deviation from this tendency at low temperatures is associated with a change in the magnetic properties of iron rather than an atomic rearrangement. As shown on the schematic in Figure 6, there is a change that occurs at 769°C upon heating and cooling. Below this temperature α-Fe is ferromagnetic while above this temperature it is paramagnetic. The temperature when this transition in magnetic properties occurs is called the Curie temperature. This paramagnetic α-Fe was originally thought to be another allotrope of iron and it was called β-Fe. However, it is now known to be simply a magnetic transition rather than a structural one. Therefore, the low temperature bcc allotrope α-Fe can be explained by considering the combined effect of the electronic and magnetic free energy on the overall free energy of the system [24].

2.3 Mo-Zr System

2.3.1 Phase Diagram

The composition range and crystal structure of the equilibrium phases in the Mo-Zr system within the temperature range considered in this study are presented in Table 2 and a phase diagram is shown in Figure 7 for reference [25].

Table 2: Composition range and crystal structure of phases present in the Mo-Zr phase diagram.

Phase	**Wt.% Zr**	**Pearson Symbol**
Mo	0 - 10	cI2
Mo_2Zr	32 - 39	cF24
β-Zr	58 - 100	cI2
α-Zr	100	hP2

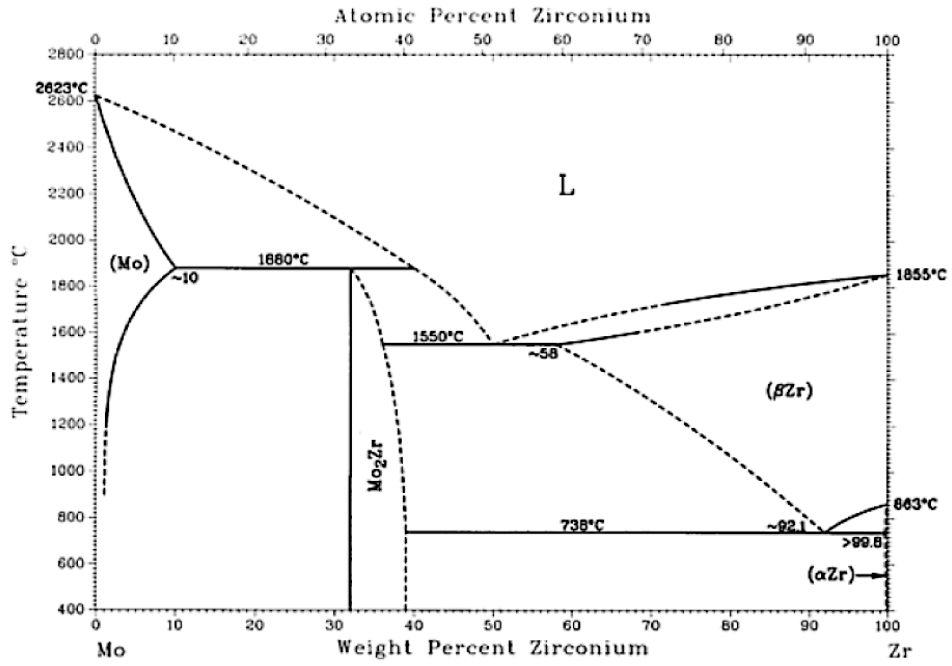

Figure 7: Binary Mo-Zr phase diagram.

The Mo-Zr phase diagram has been reviewed and presented in literature several times [26-31]. It was first presented by Hansen and Anderko in 1958 and was based largely upon previous experimental work [26]. A modified version of Hansen's compilation was later presented by Kubaschewski and von Goldbeck based on measurements obtained in further experimental work [27]. These two phase diagrams were very similar with the exception of the homogeneity range of the Mo_2Zr phase. Hansen proposed that the intermediate phase was a stoichiometric line compound while Kubaschewski claimed that it had a solubility range based on the composition range reported in literature at the time. In 1980, Brewer and Lamoreaux suggested that there was a peritectic reaction of L + Mo_2Zr → β-Zr at 1846 K contrary to the eutectic reaction previously reported [28]. However, the construction of the Mo-Zr phase diagram without the eutectic proposed by other investigators has not been accepted in the recent diffusion study by Bhatt [29]. More recently, in 2002 and 2003, thermodynamic assessments of the Mo-Zr phase diagram were conducted by Zinkevich and Perez and, respectively [30-32]. The updated phase diagrams from these two studies are presented in Figure 8.

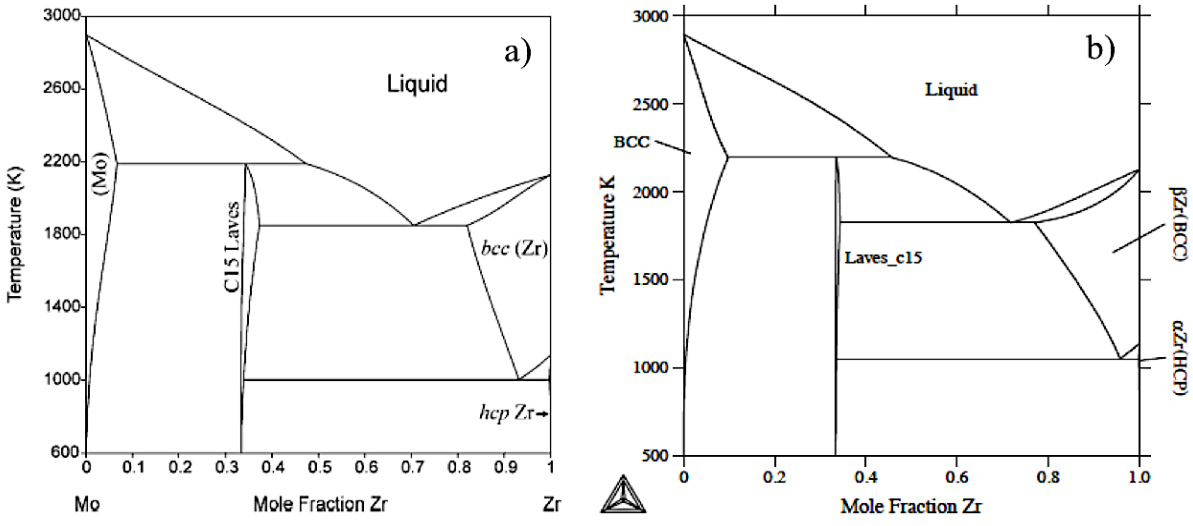

Figure 8: Updated Mo-Zr binary phase diagrams based on thermodynamic assessments presented by a) Zinkevich in 2002 and b) Perez in 2003.

The more recent assessments agree well with each other with no major discrepancies between the presented phase diagrams. According to both, Mo and Zr can substitute for each other to a rather large extent in the bcc phase while the solubility of Mo in hcp-Zr is negligible. Both also agree that there exists only one intermetallic phase, Mo_2Zr, which is formed peritectically. The fact that the homogeneity range of this intermetallic spreads over several atomic percent, however, is challenged and is suggested by both to be less than that indicated by the dotted line in Figure 7. Another feature that is notably different in the recent thermodynamic assessments is the lower solubility of Mo in bcc-Zr than indicated by the dotted line in Figure 7. These issues will be discussed with respect to the results of this work in section 5.1.

2.3.2 Diffusion Studies

Only a few reports of diffusion in the Mo-Zr system were obtained upon a literature review. Sweeny investigated diffusion in the Mo-Zr system in 1964 [33]. Intermediate phases, intended for superconductivity measurements, were prepared by diffusing Zr with Mo. Composition of the phases was estimated from electron probe measurements. The results indicated that MoZr was observed but the equilibrium phase Mo_2Zr reported by Hansen, and all investigators since, was not found in the temperature range investigated. However, MoZr does not appear as an equilibrium phase on the binary phase diagram as shown previously.

Another report of diffusion in the Mo-Zr system was based on diffusion welding of a composite with a zirconium based matrix reinforced with molybdenum wires conducted by Karpinos in 1987 [34]. Metallographic investigation following the diffusion welding revealed that interaction zones formed around the Mo fibers. The diffusion zone that formed as a result of the diffusion welding process was reported to be one-sided diffusion of Mo into Zr. According to

the study, the diffusion zone remained practically unchanged even after lengthy anneal times at 923K (650°C), while annealing at 1373K (1100°C) lead to growth of the diffusion zone and an increase in the Mo concentration in it. Based on the phase diagram and the measured compositions, the layer was determined to be a solid solution of Mo in Zr. No diffusion of Zr into Mo was observed in this study.

The most recent report of diffusion in the Mo-Zr system was provided by Bhatt in 2000 [32]. Because an observable amount of diffusion typically only occurs at high temperatures for refractory metal systems and experimentally handling low melting phases can be difficult, very little diffusion data is available in literature. However, Bhatt developed a technique for containing the liquids by melting the low melting components in a cup made of the high melting components, in this case Zr and Mo, respectively. The cup is then placed in a tungsten effusion cell and heated in an electron bombardment furnace. The sample is heated so that the required temperature is attained within 2 minutes. The sample is then furnace quenched after the predetermined anneal time at a cooling rate greater than 500K per minute. Using this method, diffusion data for both the Mo solid solution and the intermediate phase were provided for the Mo-Zr system. For the Mo-Zr system, two different anneals were conducted in this study, one at 2358K for 600 seconds to investigate diffusion in the Mo solid solution phase and the other at 2093K for 1800 seconds to investigate diffusion in the Mo_2Zr intermediate phase. The composition dependent interdiffusion coefficient for the Mo solid solution phase at 2358K was calculated to range from 1.63×10^{-13} to 1.27×10^{-14} m^2/s for Zr concentrations from 4.9 to 0 at.% respectively. The interdiffusion coefficient for the Mo_2Zr intermediate phase at 2093K was also calculated and was determined to be 8.83×10^{-14} m^2/s.

2.4 Fe-Mo System

2.4.1 Phase Diagram

The composition range and crystal structure of the equilibrium phases in the Fe-Mo system within the temperature range considered in this study are presented in Table 3 and a phase diagram is shown in Figure 9 for reference [35].

Table 3: Composition range and crystal structure of phases present in the Fe-Mo phase diagram.

Phase	**At.% Mo**	**Pearson Symbol**
α-Fe	0 - 24.4	cI2
γ-Fe	0 - 1.7	cF4
λ-Fe_2Mo	33.3	hP12
μ-Fe_7Mo_6	39 - 44	hR13
Mo	68.7 - 100	cI2

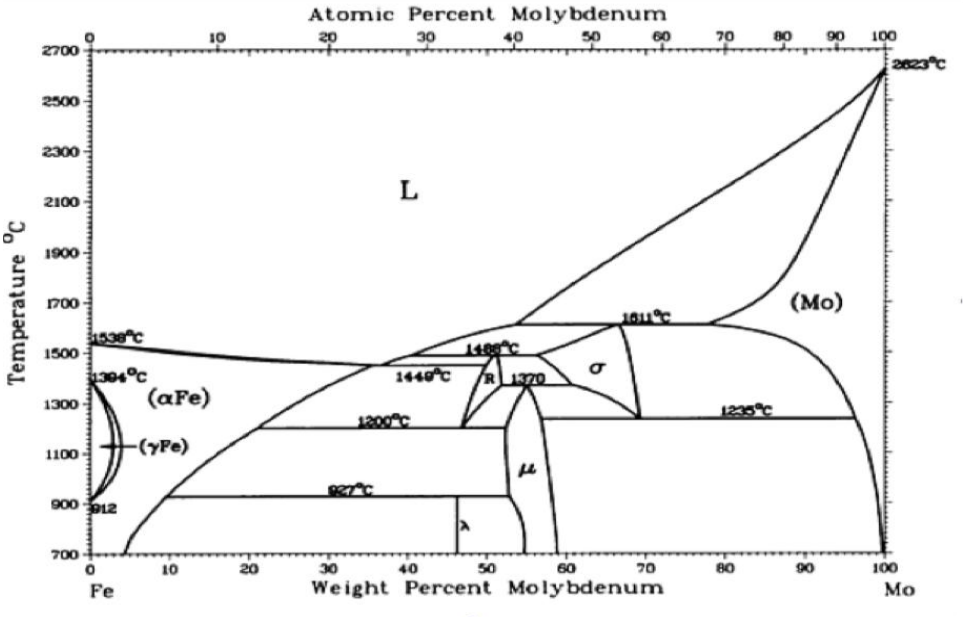

Figure 9: Binary Fe-Mo phase diagram.

The Fe-Mo phase diagram has been reviewed and presented in literature several times [26, 31, 35-37]. It was first presented by Hansen and Anderko in 1958 and was essentially based upon experimental work published before 1930 [26]. According to Hansen's version, only two intermediate phases were present, σ and μ. A modified version of Hansen's compilation was later presented in 1967 by Sinha after re-determining the Fe-rich side of the phase diagram [36]. Sinha reported a new R phase and confirmed the existence of the λ phase that had since been observed experimentally. Most investigators up to that point had not detected the λ phase however. In 1974, Heijwegen presented a phase diagram determined based on a diffusion couple analysis [37]. The λ phase was again not observed and was hence removed from that version of the phase diagram. Guillermet then published a version in 1982 based on experimental data and a thermodynamic assessment again including the λ phase [35]. Most recently, Zinkevich and Mattern provided a thermodynamic assessment of the Fe-Mo phase diagram and it agrees quite well with Guillermet's representation with the exception of slight differences in some solubility ranges [31, 38]. The earlier versions of the Fe-Mo phase diagram are presented in for reference.

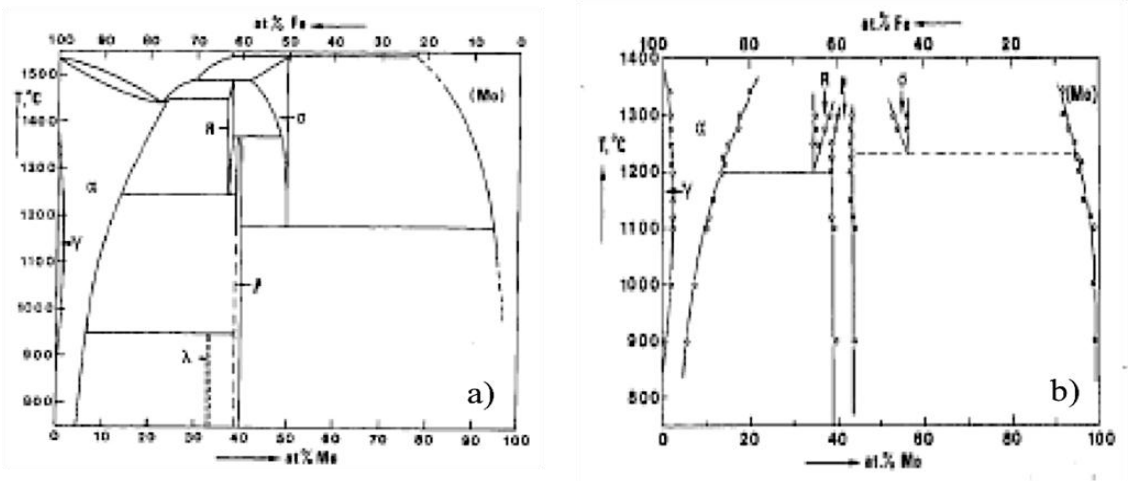

Figure 10: Early versions of Fe-Mo binary phase diagrams based on experimental work as presented by a) Sinha in 1967 and b) Heijwegen in 1974.

2.4.2 Diffusion Studies

There are two main reports in literature where the Fe-Mo system was investigated via solid-to-solid diffusion couple method [37, 39]. In the earlier study, Rawlings assembled couples between the two pure metals using mechanical bonding and annealed them at temperatures ranging from 800 to 1405°C [39]. The diffusion couples were then examined via microprobe. The authors do not mention the solid solutions phases and instead focused on the intermetallic phases that developed in the couples. In all couples, the authors reportedly observed the μ phase at about 60 at.% Fe and the R-phase at about 63 at.% Fe. They also observed very thin layers of the σ phase at and above anneal temperatures of 1255°C.

The second study, conducted by Heijwegen in 1974, used diffusion couples to determine the phase diagram as shown in Figure 10b [37]. Diffusion couples were assembled between both pure metals and binary alloys in order to investigate phase boundaries. The couples were spot welded instead of mechanically bonded prior to diffusion anneals in the temperature range of 800 to 1300°C. The concentration measurements conducted throughout this study were performed using an EPMA. According to the authors, the λ phase was not detected in any of the couples and it was suggested that this phase is only stable in the presence of other additions. Based on the diffusion couple analysis, it was determined that the R phase is stable above 1200°C. The σ phase was also determined to be a stable high temperature phase with a slightly larger homogeneity range than that suggested by Hansen. The homogeneity range of the μ phase was observed to be larger also at about 4.5 at.% Fe as compared to the 1 at.% Fe as reported by Sinha.

2.5 Fe-Zr System

2.5.1 Phase Diagram

The composition range and crystal structure of the equilibrium phases in the Fe-Zr system within the temperature range considered in this study are presented in Table 4 and a phase diagram is shown in Figure 11 for reference [40].

Table 4: Composition range and crystal structure of phases present in the Fe-Zr phase diagram.

Phase	**At.% Fe**	**Pearson Symbol**
α-Fe	99.9 - 100	cI2
$Fe_{23}Zr_6$	79.3	cF116
Fe_2Zr	66 - 73	cF24
$FeZr_2$	31 - 33.3	tI12
$FeZr_3$	24 - 27	oC16
β-Zr	0 - 7	cI2
α-Zr	0	hP2

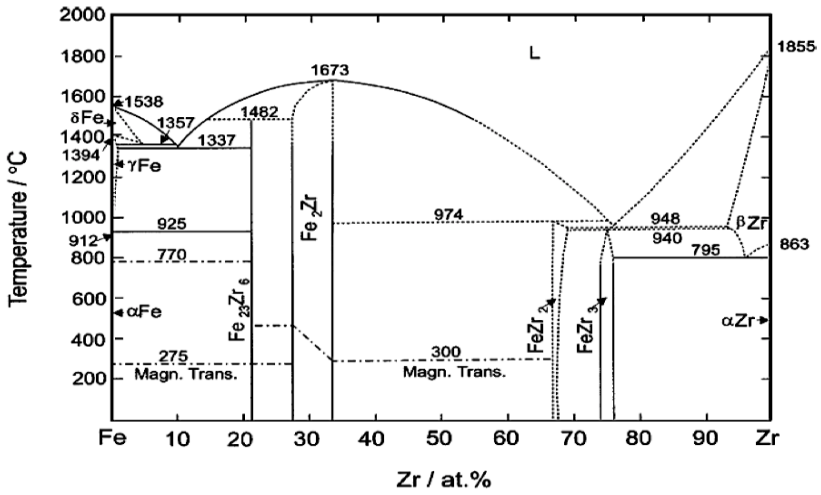

Figure 11: Binary Fe-Zr phase diagram.

The Fe-Zr phase diagram has been reviewed and presented in literature several times [40-45], as shown in Figure 12. One of the earlier versions was presented by Arias as shown in Figure 12 [41]. The key features to notice in this phase diagram are the $ZrFe_3$ phase and the high temperature Zr_2Fe phase. Another version was then published by Okamoto in 1993 showing the extension of the Zr_2Fe phase field down to room temperature and renaming the phase previously identified as Fe_3Zr as $Fe_{23}Zr_6$ [40]. Several groups investigated this $Fe_{23}Zr_6$ phase and varying results ignited controversy regarding its existence. One of the studies was conducted by Liu in 1995 in which the existence of the, then still known as the Fe_3Zr phase, was investigated via TEM imaging, electron diffraction and STEM composition analysis [46]. The phase was determined to have a composition and crystal structure belonging to the Th_6Mn_{23} prototype, hence the change in notation. Still concerned with the contradictory results obtained by several authors regarding this phase, Servant published another version of the phase diagram in 1995 based on an experimental and thermodynamic assessment [42]. The existence of the $Fe_{23}Zr_6$ phase was confirmed in this study and the phase diagram presented resembled that reported by Okamoto with smaller homogeneity ranges for the intermediate phases. Around the same time, Granovsky was also investigating the intermetallic phases in the Fe-rich region of the phase diagram via X-ray diffraction and electron microscopy [43]. The results agreed well with Okamoto's phase diagram and no significant changes were published from this study. Another experimental study was conducted by Abraham which also confirmed the existence of $Fe_{23}Zr_6$ in an Fe-9.8at.%Zr alloy [47]. In 2001 Jiang published a phase diagram based on thermodynamic calculations that looked similar to Servant's [44]. The most recent phase diagram was published by Stein in 2002. The $Fe_{23}Zr_6$ phase was again removed because Stein suggested that it was not an equilibrium phase in the binary system and was oxygen stabilized.

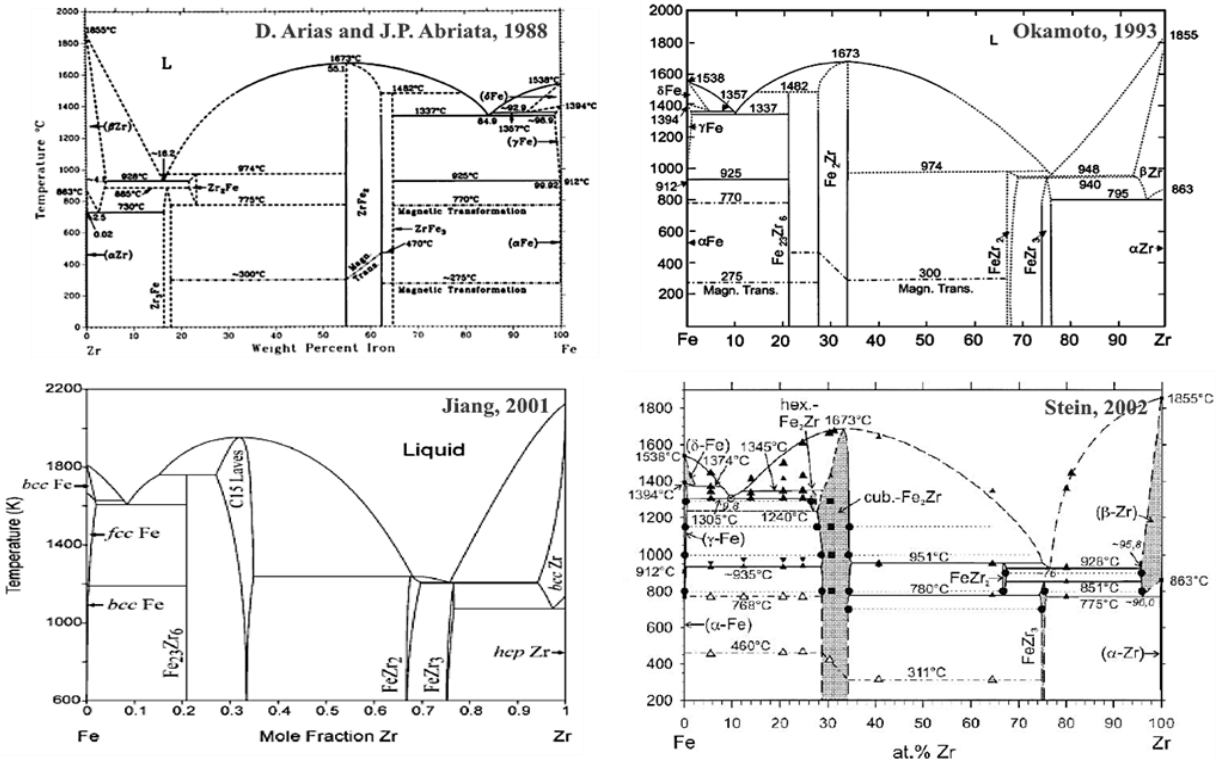

Figure 12: Various versions of the Fe-Zr phase diagram based on thermodynamic calculations and experimental values.

2.5.2 Diffusion Studies

A few studies regarding diffusion in the Fe-Zr system have been reported [33, 48, 49]. In 1964 Sweeney observed the Fe_2Zr, $FeZr_2$, and $FeZr_3$ intermetallics when Zr was diffused with Fe to form intermediate phases for superconductivity measurements [33]. A study conducted by Harada in 1986 confirmed the presence of $FeZr_3$ in the diffusion zone at the interface of Fe and Zr thin films annealed below 1273K [48]. The most relevant study was conducted by Bhanumurthy in 1991 when a more traditional diffusion couple study was performed. The results of this investigation showed that $FeZr_3$ formed in couples annealed at and above 1134K, Fe_2Zr, $FeZr_2$, and $FeZr_3$ all formed in the couple annealed at 1213K and no intermetallics formed in couples annealed in the temperature range of 973 to 1073K [49].

CHAPTER 3: METHODOLOGY

3.1 Diffusion Couple Experiments

The interdiffusion behavior in the Mo-Zr, Fe-Mo, and Fe-Zr systems was investigated via solid-to-solid diffusion couples. One-half inch diameter rods of 99.9% pure Mo, 99.9% pure Fe, and 99.2% pure Zr were acquired from Alfa Aesar™. These rods were cross-sectioned into disks approximately 2 to 3 millimeters in thickness. After being cross-sectioned, the disks were mounted in epoxy and metallographically polished down to 1200 grit surface finish using silicon carbide (SiC) grinding paper and ethanol as a lubricant. Following polishing, the disks were removed from the epoxy mounts and placed in ethanol in order to mitigate further oxidation. The polished surfaces of the disks were then mechanically bonded through assembly into a stainless steel jig consisting of one inch diameter plates, three screws, and three nuts with two alumina disks in between the metals of interest and the steel plates that served as spacers to prevent them from bonding to each other once raised to the anneal temperature as schematically shown in Figure 13. The two metal disks of interest were also polished once again at 1200 grit immediately before assembly to ensure that any native oxide scale was removed before final assembly.

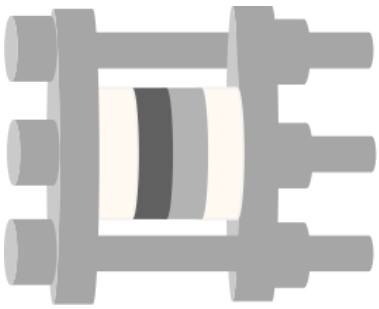

Figure 13: Schematic of a solid-to-solid diffusion couple assembly including stainless steel jig, alumina spacers, and two metal disks of interest.

Once assembled, the entire jig was placed in a quartz capsule, as shown in Figure 14, designed specifically for the diffusion couple to be sealed under vacuum or an inert atmosphere to prevent oxidation at high temperatures. A piece of tantalum foil was also placed in each quartz capsule to serve as an oxygen getter to further prevent oxidation due to the presence of any residual oxygen in the capsule after being sealed. The cap was then sealed on the capsule using an oxy-fuel welding torch. Immediately after the cap was fully sealed, the entire capsule was attached to the vacuum system shown in Figure 15 and evacuated to a rough vacuum. The capsule was then flushed a minimum of three times with ultra-high purity argon and hydrogen to getter any remaining oxygen. Finally, the capsule was evacuated to a high vacuum of 9×10^{-6} torr or below before the capsule was completely sealed using the oxy-fuel torch. Each diffusion couple was then isothermally annealed in a pre-heated Lindberg/Blue™ three-zone tube furnace, shown in Figure 16, for the predetermined time. An experimental matrix detailing the anneal temperatures and times for each couple is presented in Table 5 for reference.

After the anneal time had elapsed, the capsules were removed from the furnace and quenched in a bucket of room temperature water and immediately broken open so the diffusion couple itself cooled as quickly as possible. The diffusion couple jig was then removed from the quench water and allowed to dry. Once dry, the entire jig assembly was mounted in epoxy and allowed to cure overnight. The diffusion couple was then cut out of the jig by sectioning through the alumina spacer and the three screws on each side of the couple using an Allied™ low speed saw using a diamond wafering blade and an oil lubricant. Only the couple was then remounted in epoxy and cross-sectioned perpendicular to the interface. One half of the couple was then metallographically polished down to a 3 μm surface finish using a combination of SiC grinding paper and oil-based diamond compound.

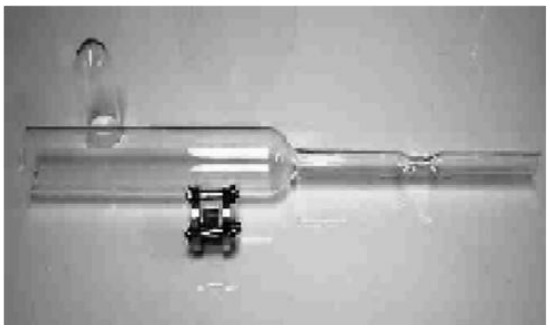

Figure 14: Quartz capsule designed for encapsulation of diffusion couple under vacuum or inert atmosphere to prevent oxidation during high temperature anneal.

Figure 15: Vacuum system used during encapsulation of diffusion couples for evacuation and purging with inert gas.

Figure 16: Lindberg/Blue™ three-zone tube furnace used for high temperature annealing of diffusion couples.

Table 5: Experimental diffusion couple matrix detailing anneal temperatures and times.

Diffusion Couple		Temperature (°C)	Anneal Time (days)	Anneal Time (hours)
Side 1	**Side 2**			
Mo	Zr	700	60	1440
		750	30	720
		850	15	360
		950	15	360
		1000	15	360
		1050	15	360
Fe	Mo	650	60	1440
		750	30	720
		850	15	360
		850	30	720
		900	30	720
		1000	15	360
		1050	3	72
			5	120
			8	192
			15	360
Fe	Zr	750	30	720
		850	15	360

3.2 Interdiffusion Zone Characterization

Once the diffusion couples were polished, optical microscopy was used to verify the bond quality between the two metal specimens. If well bonded, a Zeiss™ Ultra-55 FEG SEM operated at 20 kV accelerating voltage was then employed to characterize the microstructure of the interdiffusion zone (IDZ). The backscatter electron (BSE) imaging mode was used to obtain compositional contrast to distinguish the various phases present. With the sample at a working distance of 13 mm, EDS point analysis was used to identify the phase constituents within the IDZ. Also, preliminary line scans were performed using EDS to determine whether or not there were concentration gradients present in each of the layers. The Mo L-α, Zr L-α, and Fe K-α energy peaks were used for quantification of the EDS spectra.

For the diffusion couples with a large enough IDZ thickness and concentration gradient, only the high temperature Mo vs. Zr couples in this case, EPMA was conducted using a JEOL™ Superprobe 733 to obtain concentration profiles for quantitative analysis. The line scans were collected using an accelerating voltage of 20 kV and a point-to-point step size of 5 μm. The pure Mo and Zr at the terminal ends of one of the diffusion couples were used as calibration standards. Again, the Mo L-α and Zr L-α X-ray lines were used for quantification. The ZAF correction factor technique was employed to convert X-ray intensities to concentration where Z corresponds to an atomic number correction, A relates to an absorption correction, and F corresponds to a fluorescence correction. Once the concentrations were calculated, the values were normalized to 100%. The concentration profiles reported for each couple were based on the normalized atomic percentages and were then utilized to calculate the interdiffusion coefficients as a function of temperature and concentration.

3.3 Quantitative Analysis

3.3.1 Growth Constants

For diffusion couples in which intermetallic layers developed, a parabolic growth constant was calculated assuming that the formation of the layer was diffusion controlled. In order to calculate these growth constants, the BSE micrographs that were collected from each couple were used to conduct thickness measurements. The "measure" tool in the ImageJ program was used to obtain thickness values of each layer in units of pixels. Using the scale bar in each image, a conversion factor was obtained to convert the thickness to units of micrometers. A minimum of ten measurements were performed for each intermetallic layer in order to obtain a statistical average and standard deviation.

Once the thickness values were obtained, the parabolic growth constants were calculated based on the average thickness measured for each of the layers using

$$k_p = \frac{Y^2}{2t} \tag{16}$$

where k_p is the parabolic growth constant, Y is the layer thickness in meters, and t is the anneal time in seconds. The calculated growth constants can then be compared to determine the relative rates at which each of the phase layers develop within the interdiffusion zone. Also, the growth constants obtained can be used to calculate the pre-exponential factor and activation energy for growth of each of the phases, which can then be used to calculate the growth rate at any temperature as shown in section 3.3.3.

3.3.2 Interdiffusion Coefficients

For the high temperature (850 to 1050°C) Mo vs. Zr diffusion couples, interdiffusion coefficients were calculated based on the measured concentration profiles. The normalized Mo concentration, in atomic percent, was plotted as a function of distance to obtain the original concentration profile for each diffusion couple. The normalized data was then fitted to an exponential growth curve using the nonlinear fit tool in Origins 8. Once the fitted data was obtained, it was used to calculate the interdiffusion flux and interdiffusion coefficient as a function of composition via the Boltzmann-Matano method. In this method, the location of the Matano plane, or the plane of mass balance, is determined by numerically integrating over the concentration profile so as to satisfy

$$\int_{C_i^{+\infty}}^{C_i^o} x dC_i + \int_{C_i^o}^{C_i^{-\infty}} x dC_i = 0 \tag{17}$$

where x is distance, C_i is the concentration of component i (Mo or Zr in this case) at that point, C_i^o is the concentration of component i at the Matano plane, and $C_i^{-\infty}$ and $C_i^{+\infty}$ are the concentrations of component i at the terminal ends of the couple. The graphical representation of this is shown in Figure 17. The Matano plane, x_o , is defined by the position that makes the two horizontally hatched areas in Figure 17 equal. The interdiffusion flux of component i, $\widetilde{J_\imath}$, is then calculated with respect to the position of the Matano plane and is given by

$$\widetilde{J_\imath} = \frac{1}{2t}\int_{C_i^{\pm\infty}}^{C_i}(x - x_o)\, dC_i \tag{18}$$

By combining the flux equation with Fick's first law, the interdiffusion coefficient, $\widetilde{D}_\iota$, can be calculated using

$$\widetilde{D}_\iota = \frac{\frac{1}{2t}\int_{C_i^{+\infty}}^{C_i}(x-x_o)dC_i}{\frac{dC_i}{dx}} \tag{19}$$

Using this technique, concentration dependent diffusion coefficients were calculated for each of the Mo vs. Zr concentration profiles obtained from the couples annealed at temperatures between 850 and 1050°C. The diffusion coefficients obtained can then be used to calculate the pre-exponential factor and activation energy for interdiffusion, which are then used to calculate the diffusion coefficient at any temperature as shown in section 3.3.3.

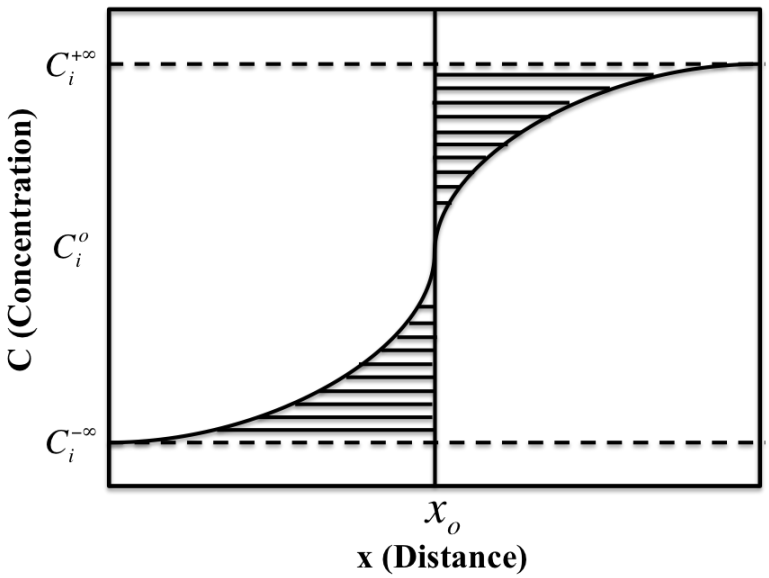

Figure 17: Schematic concentration profile for component i in a hypothetical diffusion couple between two alloys with starting compositions $C_i^{-\infty}$ and $C_i^{+\infty}$ showing the location of the Matano plane x_o where the hatched areas on either side are equal.

3.3.3 Activation Energies and Pre-exponential Factors

Temperature dependent processes generally follow an Arrhenius relationship. Since diffusion is a thermally activated process, the temperature dependence of both parabolic growth constants and diffusion coefficients should take the form of Arrhenius equations given by

$$k_p = k_o \exp\left(\frac{-Q_k}{RT}\right) \quad \text{and} \quad \widetilde{D_i} = \widetilde{D_o} \exp\left(\frac{-Q_d}{RT}\right) \tag{20}$$

respectively, where k_o and $\widetilde{D_o}$ are pre-exponential factors in m^2/s, Q_k and Q_d are the activation energies for growth and diffusion in J/mole, R is the molar gas constant in J/mole-K, and T is the anneal temperature in Kelvin. The activation energies and pre-exponential factors can therefore be determined from the slope and intercept of the line formed by plotting the natural log of either k_p and $\widetilde{D_i}$ versus the inverse temperature as shown in Figure 18.

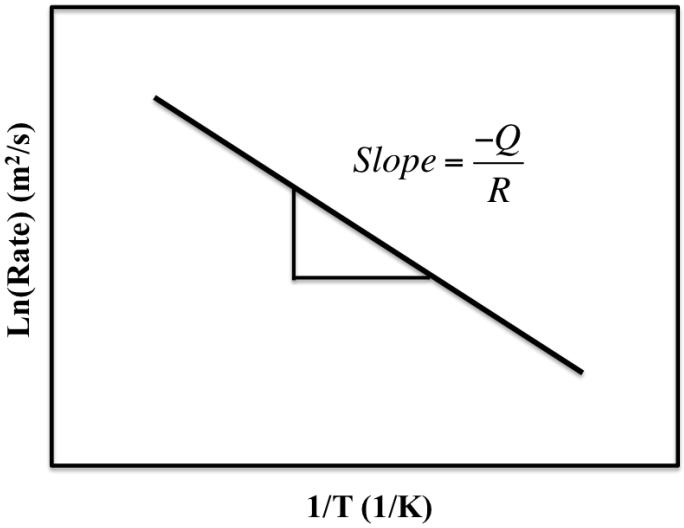

Figure 18: Schematic Arrhenius plot showing how activation energy and pre-exponential factor for parabolic growth or diffusion can be obtained.

CHAPTER 4: RESULTS

4.1 Mo vs. Zr Diffusion Couples

Several diffusion couples were assembled between Mo and Zr and were annealed at the temperatures and times listed in Table 6. The binary Mo-Zr phase diagram is also repeated here in Figure 19 with dotted lines indicating the anneal temperatures. Some important features of the phase diagram are the high solubility of Mo in Zr at high temperatures and the negligible solubility of both Zr in Mo and Mo in Zr at low temperatures, the existence of one intermediate phase, Mo_2Zr, with a relatively high homogeneity range, and the allotropic transformation of Zr from hcp to bcc at 863°C. The anneal temperatures were specifically chosen to investigate the effect of the allotropic transformation of Zr on the interdiffusion behavior between Mo and Zr. The times were determined based on a preliminary study conducted at 850°C.

Table 6: Experimental diffusion couple matrix for the Mo-Zr system.

Diffusion Couple		**Temperature (°C)**	**Anneal Time (days)**
Side 1	**Side 2**		
Mo	Zr	700	60
Mo	Zr	750	30
Mo	Zr	850	15
Mo	Zr	950	15
Mo	Zr	1000	15
Mo	Zr	1050	15

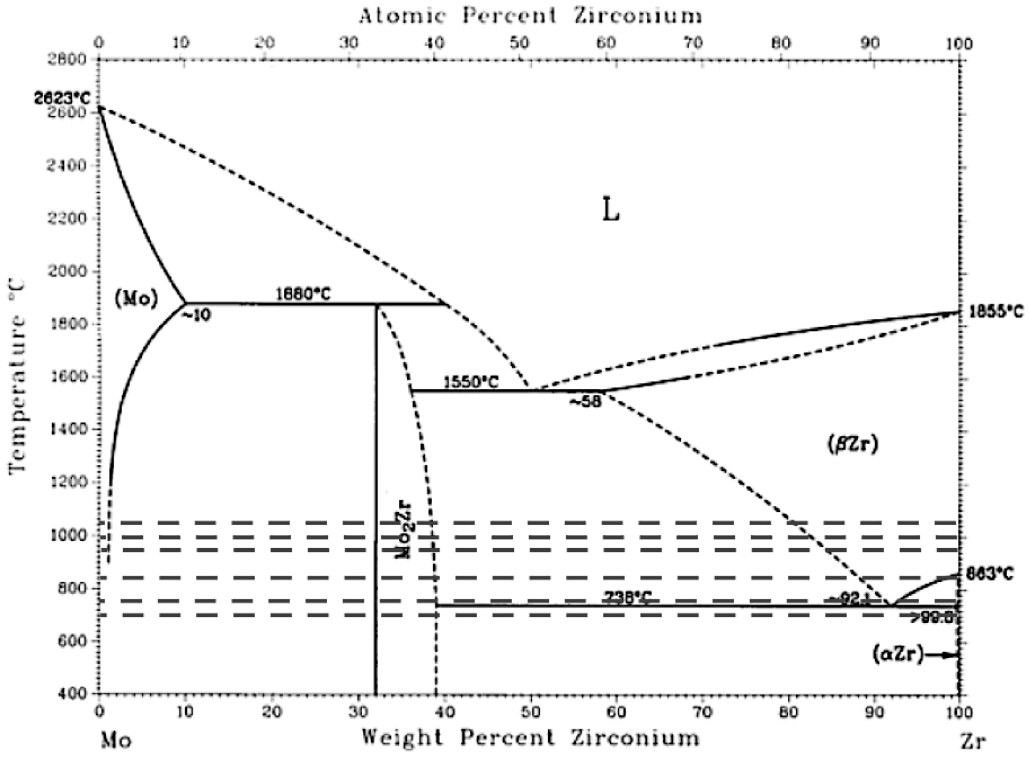

Figure 19: Binary Mo-Zr phase diagram with dotted lines representing anneal temperatures.

4.1.1 Interdiffusion Zone Microstructure

Typical backscatter electron micrographs of the interdiffusion zones that developed in each of the Mo vs. Zr diffusion couples are presented in Figure 20 through Figure 25. The corresponding concentration profiles are superimposed on each micrograph for clarity. At first glance, it appears that in the couples annealed above 700°C there is only a large region of Zr solid solution. However, in each couple, there is a thin layer at the interface that was identified via EDS as Mo_2Zr. In the couple annealed at 700°C two layers were observed including a thin Mo_2Zr layer and a larger layer with a relatively constant composition of approximately 6 at.% Mo. This result was not expected based on the binary Mo-Zr phase diagram as it indicates that there is negligible solubility of Mo in Zr at temperatures below 738°C.

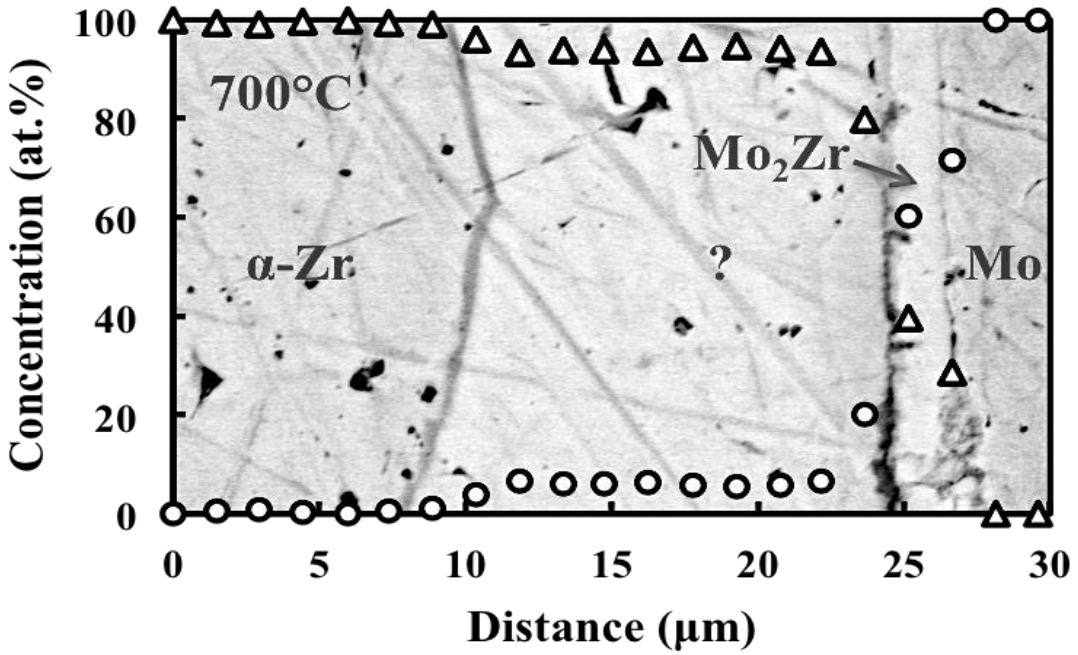

Figure 20: BSE micrograph and superimposed concentration profile of Mo vs. Zr diffusion couple annealed at 700°C for 60 days.

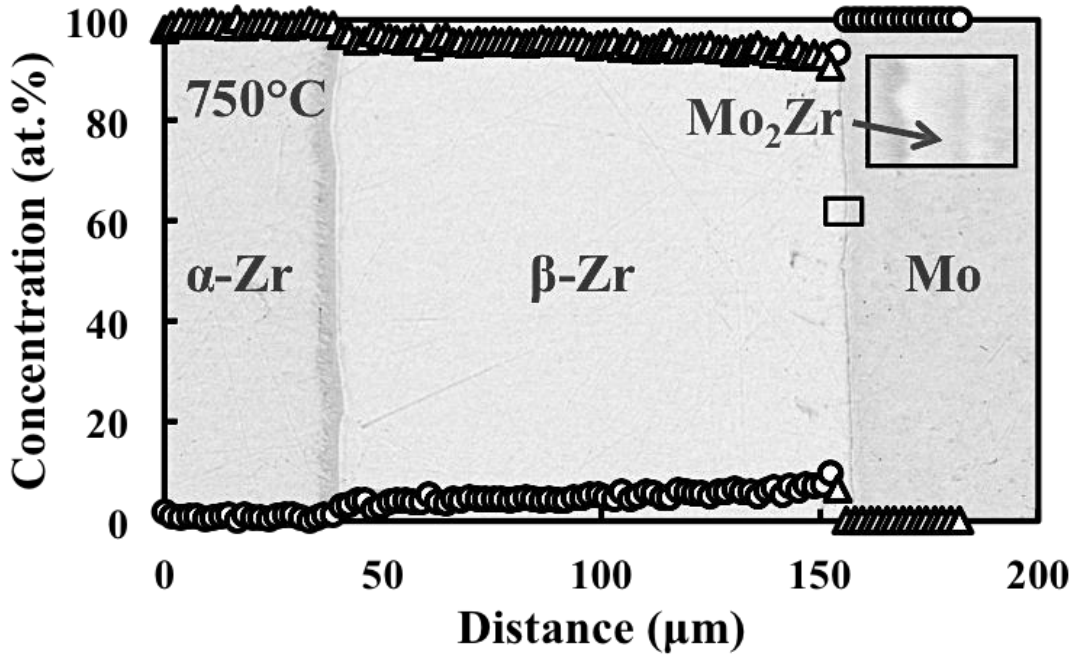

Figure 21: BSE micrograph and superimposed concentration profile of Mo vs. Zr diffusion couple annealed at 750°C for 30 days.

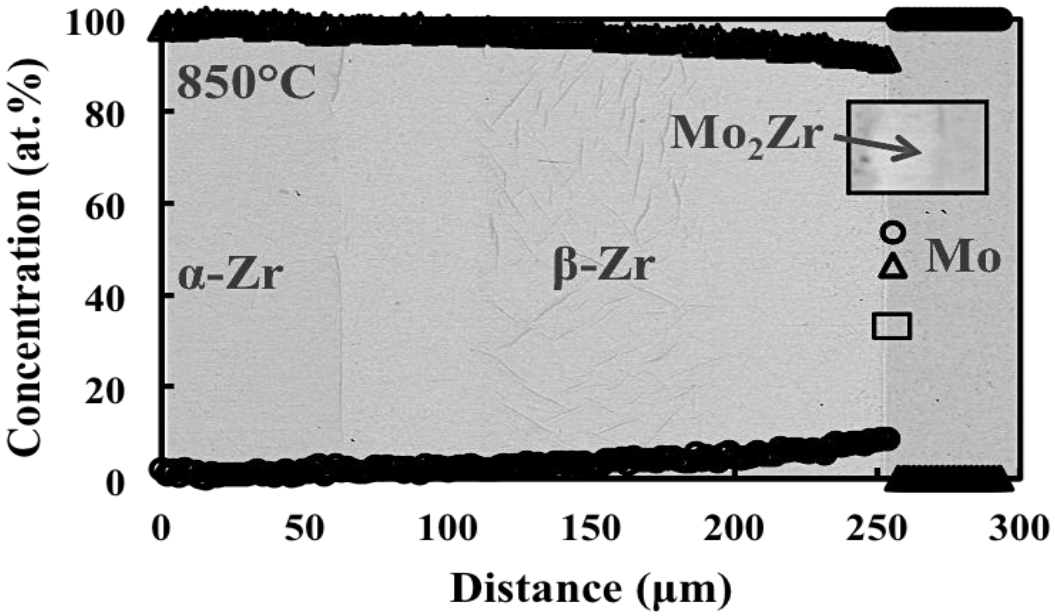

Figure 22: BSE micrograph and superimposed concentration profile of Mo vs. Zr diffusion couple annealed at 850°C for 15 days.

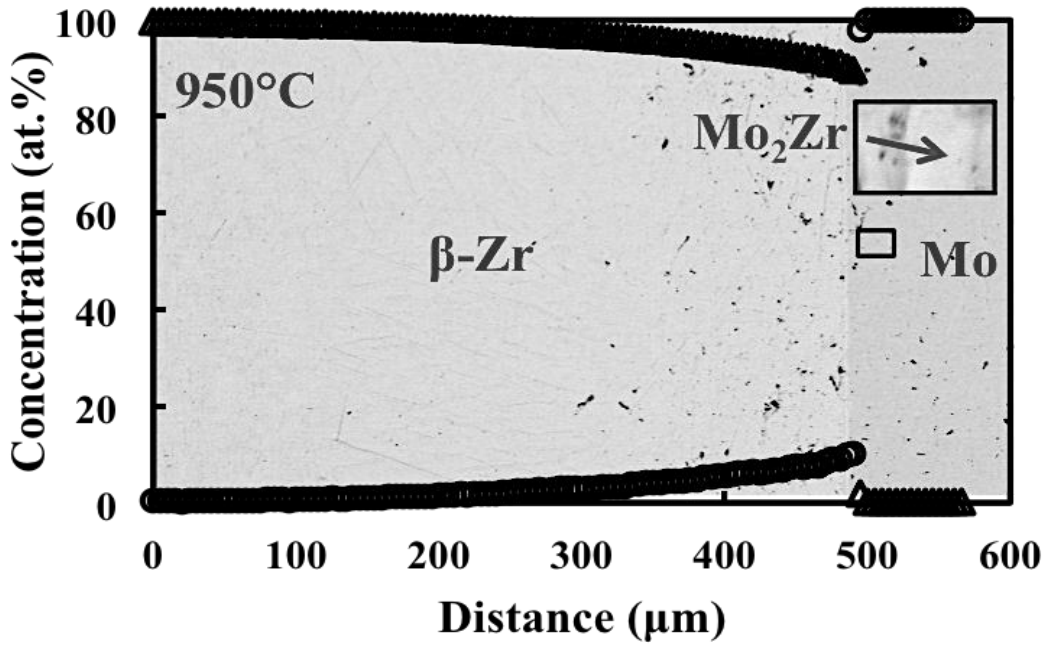

Figure 23: BSE micrograph and superimposed concentration profile of Mo vs. Zr diffusion couple annealed at 950°C for 15 days.

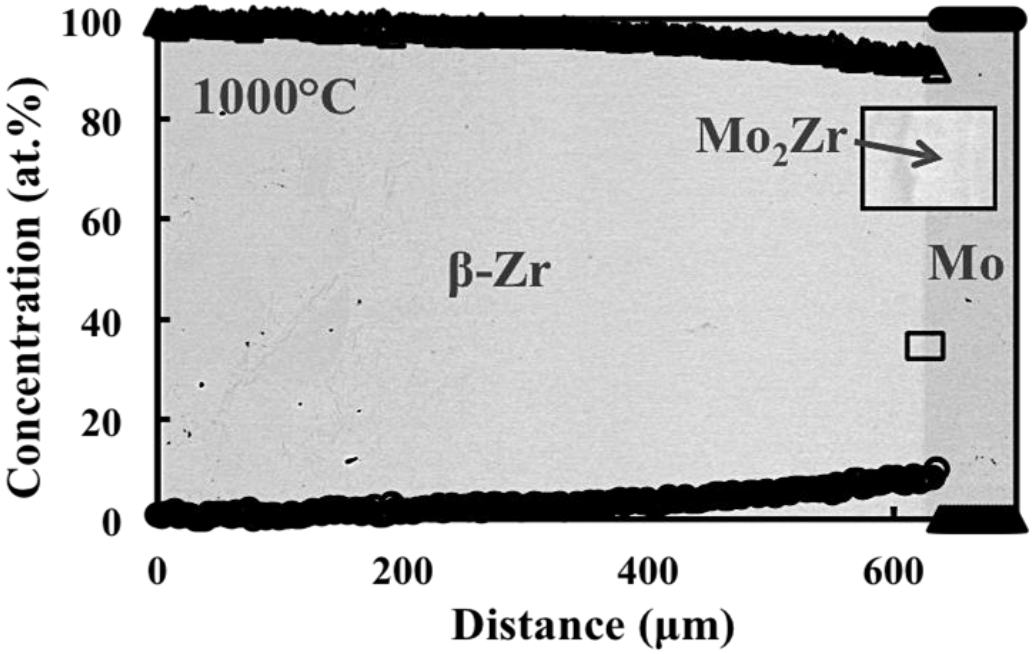

Figure 24: BSE micrograph and superimposed concentration profile of Mo vs. Zr diffusion couple annealed at 1000°C for 15 days.

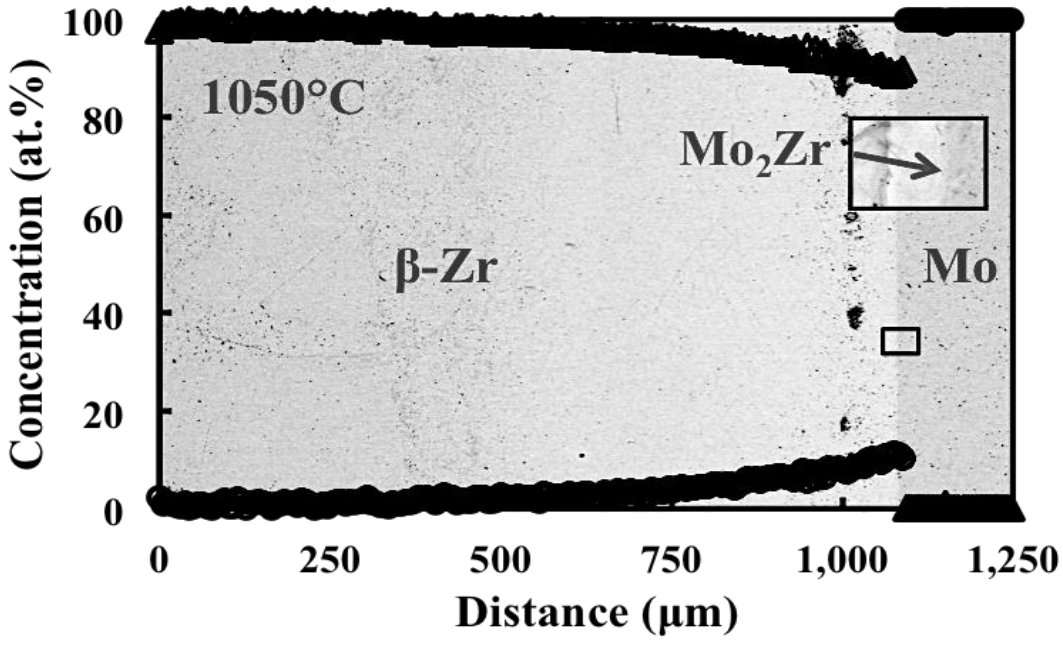

Figure 25: BSE micrograph and superimposed concentration profile of Mo vs. Zr diffusion couple annealed at 1050°C for 15 days.

4.1.2 Intermetallic Growth Kinetics

Based on the measured thicknesses of the Mo_2Zr layers, the parabolic growth constants were calculated for each diffusion couple. The average thickness determined from ten measurements and the calculated growth constant values are presented in Table 7 for each of the diffusion anneal temperatures. The growth constants calculated for the couples annealed above 700°C obey an Arrhenius relationship as shown in Figure 26. Therefore, the pre-exponential factor and activation energy for growth were determined to be approximately 6.5×10^{-15} m^2/s and 90 kJ/mole, respectively. The growth constant calculated for the Mo_2Zr layer that developed in the 700°C diffusion couple is slightly higher than expected based on the Arrhenius trend. This discontinuity in the Arrhenius trend line suggests that the allotropic transformation of Zr may affect the growth rate of the Mo_2Zr phase.

Table 7: Thicknesses and parabolic growth constants calculated for the Mo_2Zr layer that developed in the Mo vs. Zr diffusion couples.

Anneal Temp. (°C)	**Thickness (μm)**	**k_p (m^2/s)**
700	1.6	2.3×10^{-19}
750	0.8	1.4×10^{-19}
850	1.0	3.6×10^{-19}
950	1.5	8.3×10^{-19}
1000	1.6	9.4×10^{-19}
1050	2.1	1.8×10^{-18}

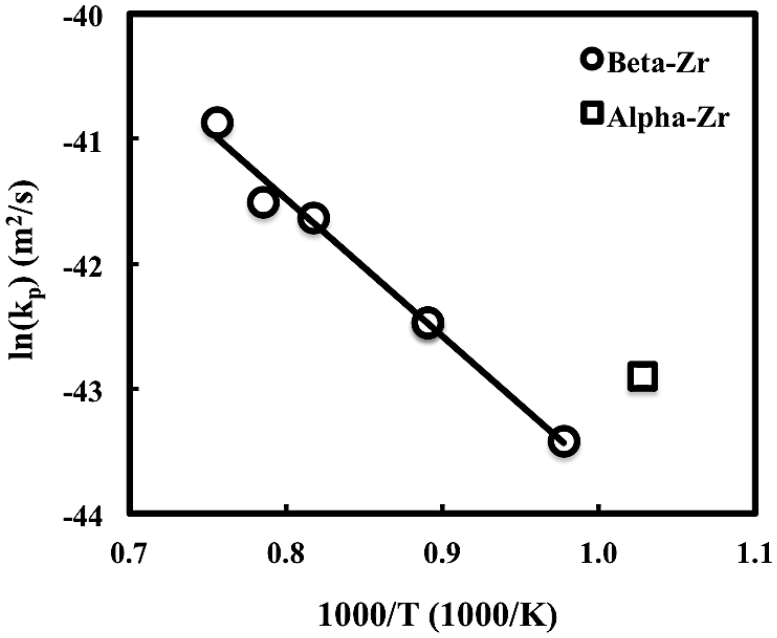

Figure 26: Arrhenius plot of parabolic growth constants calculated for Mo_2Zr.

4.1.3 Interdiffusion Coefficients

Concentration dependent interdiffusion coefficients were calculated for the Zr solid solution phase that developed in the Mo vs. Zr couples annealed between 850 and 1050°C using the Boltzmann-Matano method. The calculated interdiffusion coefficients are presented as a function of Mo concentration in Figure 27. This suggests that the interdiffusion coefficient decreases exponentially as a function of the atomic fraction of Mo in the Zr solid solution. At a constant Mo concentration of 6 at. %, the natural logarithm of the interdiffusion coefficients were plotted as a function of inverse temperature to obtain the Arrhenius plot shown in Figure 28. Based on this plot, the pre-exponential factor and activation energy for diffusion in the Zr solid solution phase were determined to be approximately 3.8 x 10^{-8} m^2/s and 150 kJ/mole, respectively.

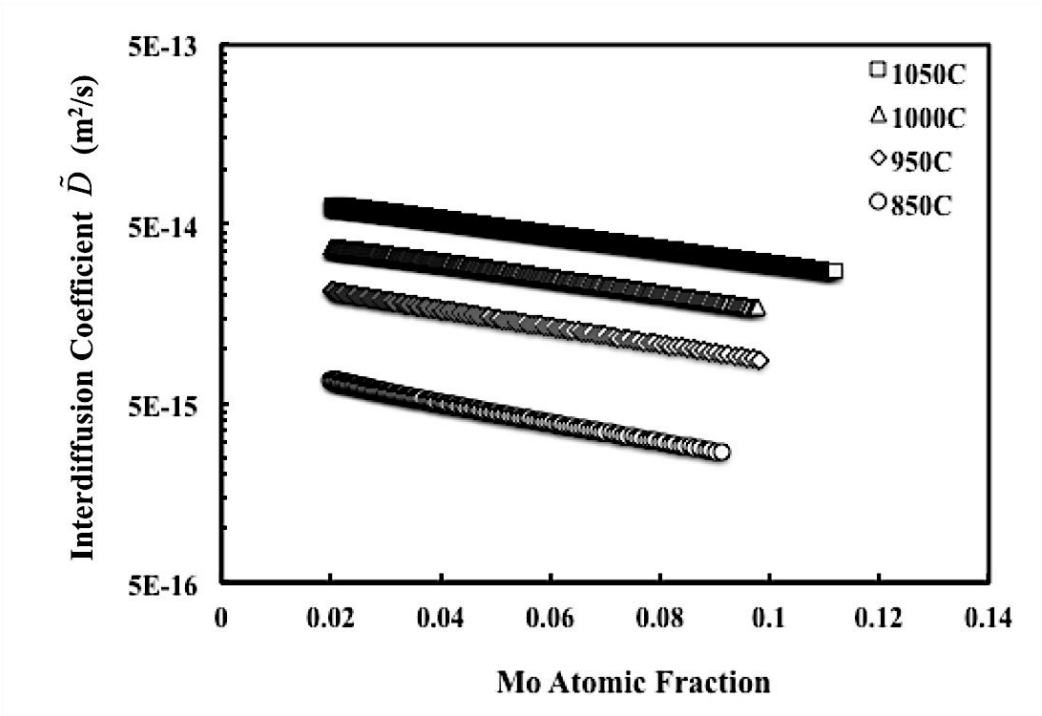

Figure 27: Concentration dependence of interdiffusion coefficients calculated for Mo vs. Zr couples annealed at 850, 950, 1000, and 1050°C for 15 days.

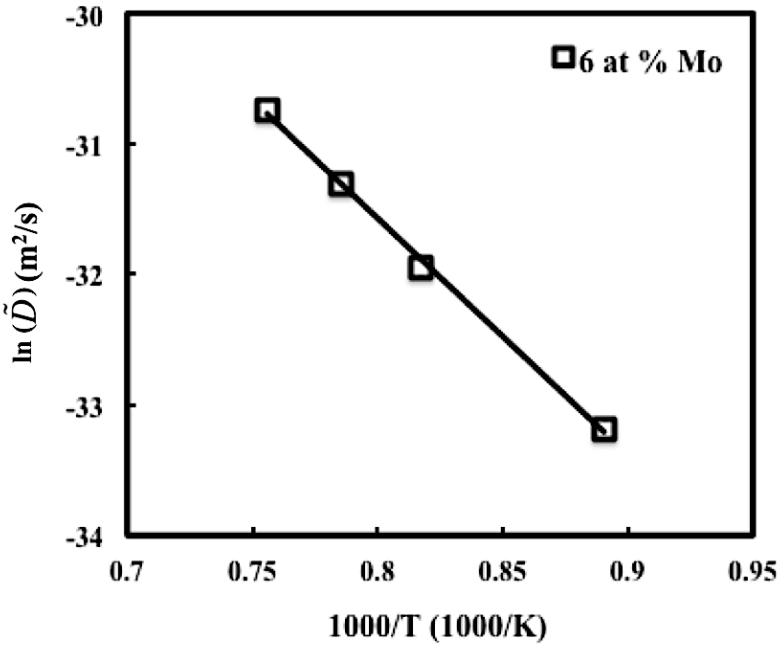

Figure 28: Arrhenius plot of interdiffusion coefficients calculated at 6 at.% Mo.

4.2 Fe vs. Mo Diffusion Couples

Several diffusion couples were assembled between Fe and Mo and were annealed at the temperatures and times listed in Table 8. The binary Fe-Mo phase diagram is also repeated here in Figure 29 with dotted lines indicating the anneal temperatures. Some important features of the phase diagram are the high solubility of Mo in Fe and the negligible solubility of Fe in Mo, the existence of two intermediate phases, λ-Fe_2Mo and μ-Fe_7Mo_6 , and the allotropic transformation of Fe from bcc to fcc at 912°C. The anneal temperatures were specifically chosen to investigate the effect of the allotropic transformation of Fe on the interdiffusion behavior between Fe and Mo. The times were determined based on preliminary results of the higher temperature couples.

Table 8: Experimental diffusion couple matrix for the Fe-Mo system.

Diffusion Couple		**Temperature (°C)**	**Anneal Time (days)**
Side 1	**Side 2**		
Fe	Mo	650	60
Fe	Mo	750	30
Fe	Mo	850	15
Fe	Mo	850	30
Fe	Mo	900	30
Fe	Mo	1000	15
Fe	Mo	1050	3
Fe	Mo	1050	5
Fe	Mo	1050	8
Fe	Mo	1050	15

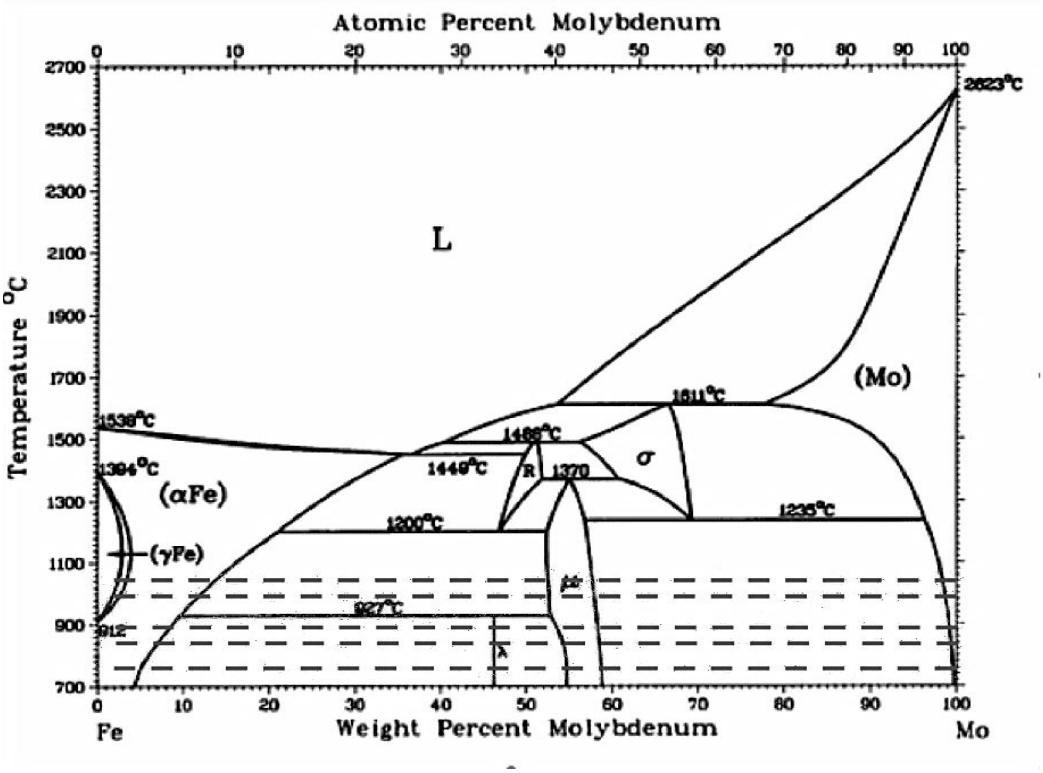

Figure 29: Binary Fe-Mo phase diagram with dotted lines representing anneal temperatures.

4.2.1 Interdiffusion Zone Microstructure

Typical backscatter electron micrographs of the interdiffusion zones that developed in each of the Fe vs. Mo diffusion couples are presented in Figure 30 through Figure 39. The corresponding concentration profiles are superimposed on each micrograph, except for the couples annealed at 650 and 750°C because the layers were too thin to obtain a meaningful concentration profile. In each couple annealed from 650 to 900°C there are two layers present that were identified as λ-Fe_2Mo and μ-Fe_7Mo_6 based on compositional data obtained via EDS and the binary phase diagram. In the two couples annealed at 850°C, in addition to the λ-Fe_2Mo and μ-Fe_7Mo_6 layers, there was a layer observed with a relatively constant composition of approximately 4 at.% Mo. This result was not expected based on the binary Fe-Mo phase

diagram as it indicates that there is significant solubility, approximately 4 at.%, of Mo in Fe at 850°C suggesting that the concentration profile should be smooth within this solid solution phase and it should not appear as a separate layer with constant composition. At the anneal temperatures of 1000 and 1050°C only the μ-Fe_7Mo_6 intermediate phase was observed as expected based on the phase diagram since the λ-Fe_2Mo is not stable above 927°C. In these couples a region of Fe solid solution was observed and identified as α-Fe while the terminal end was identified as γ-Fe based on the compositions determined via EDS and the phase diagram. There was a series of diffusion couples annealed at 1050°C for various times to investigate the growth of the μ-Fe_7Mo_6 and the α-Fe layers as a function of time. The quantitative results are presented in section 4.2.2.

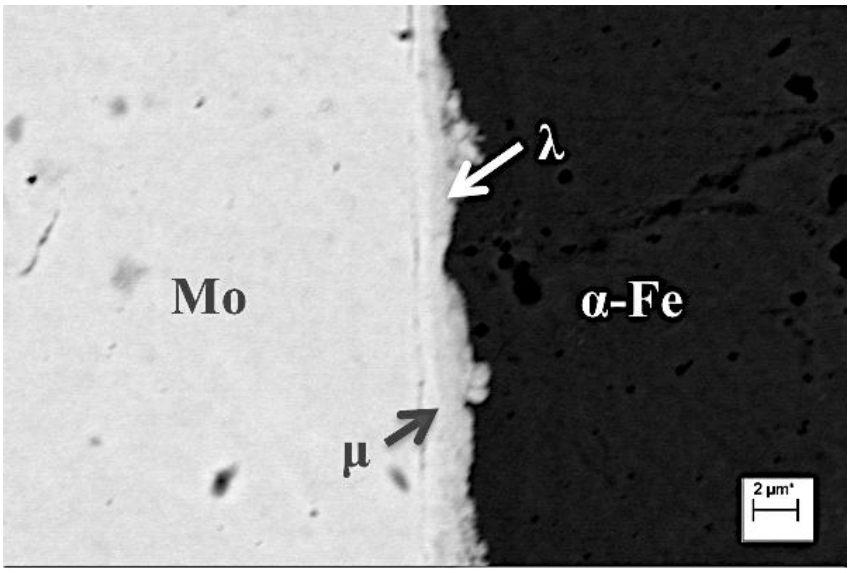

Figure 30: BSE micrograph of Fe vs. Mo diffusion couple annealed at 650°C for 60 days.

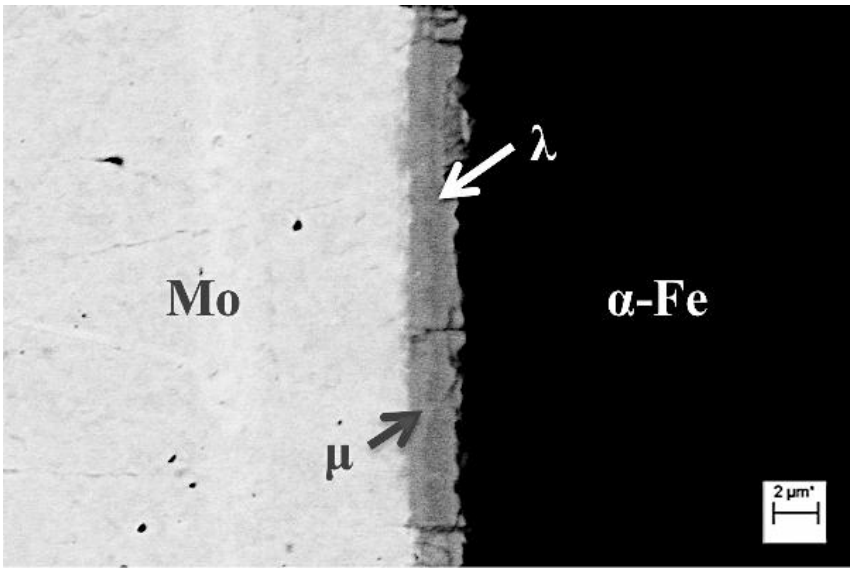

Figure 31: BSE micrograph of Fe vs. Mo diffusion couple annealed at 750°C for 30 days.

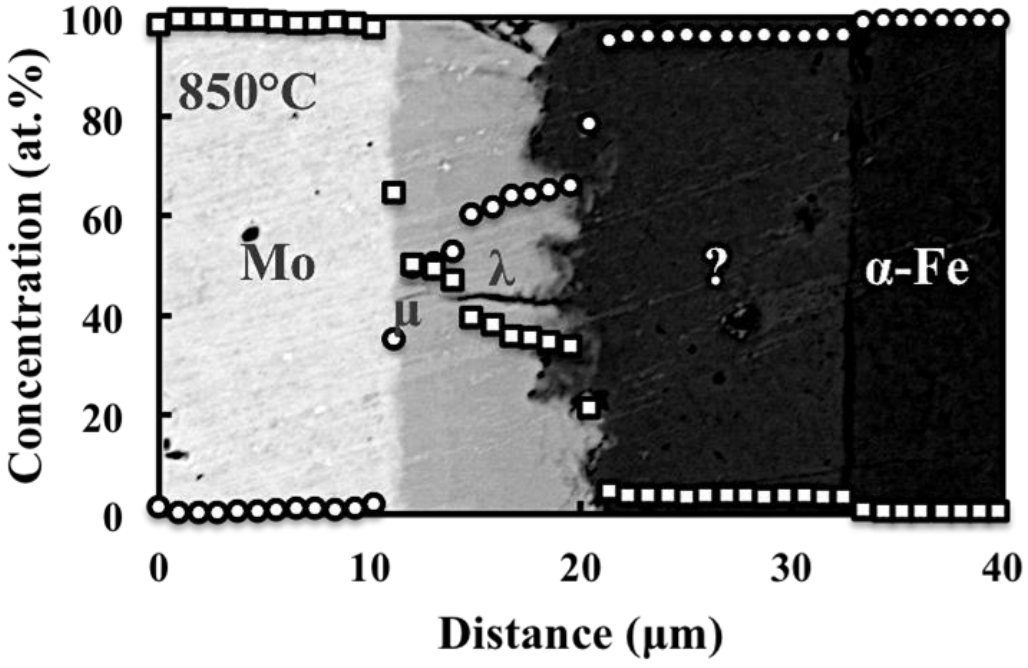

Figure 32: BSE micrograph and superimposed concentration profile of Fe vs. Mo diffusion couple annealed at 850°C for 15 days.

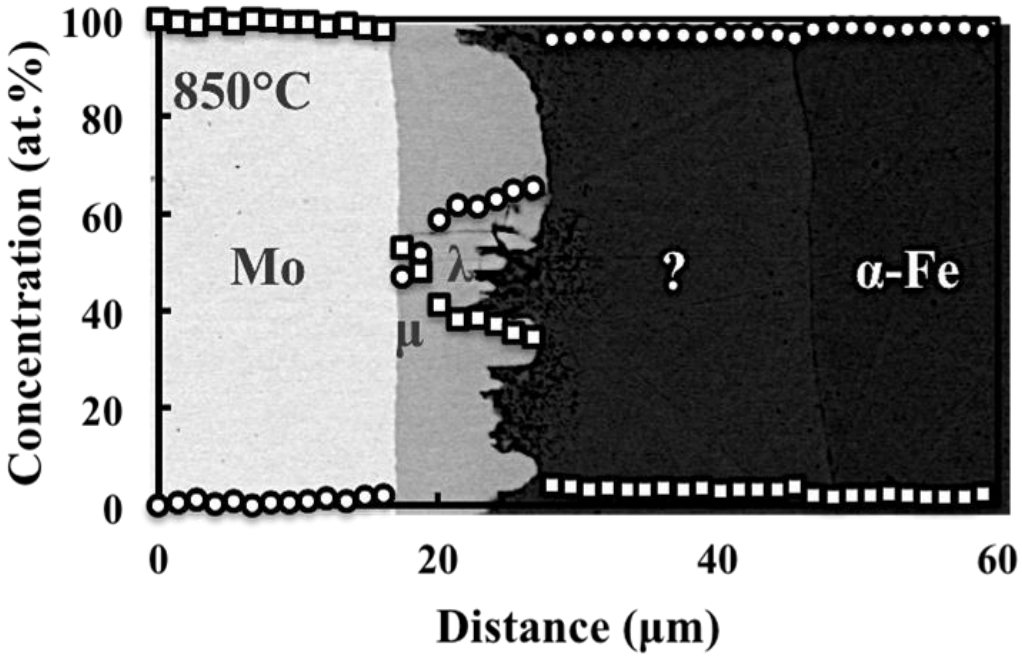

Figure 33: BSE micrograph and superimposed concentration profile of Fe vs. Mo diffusion couple annealed at 850°C for 30 days.

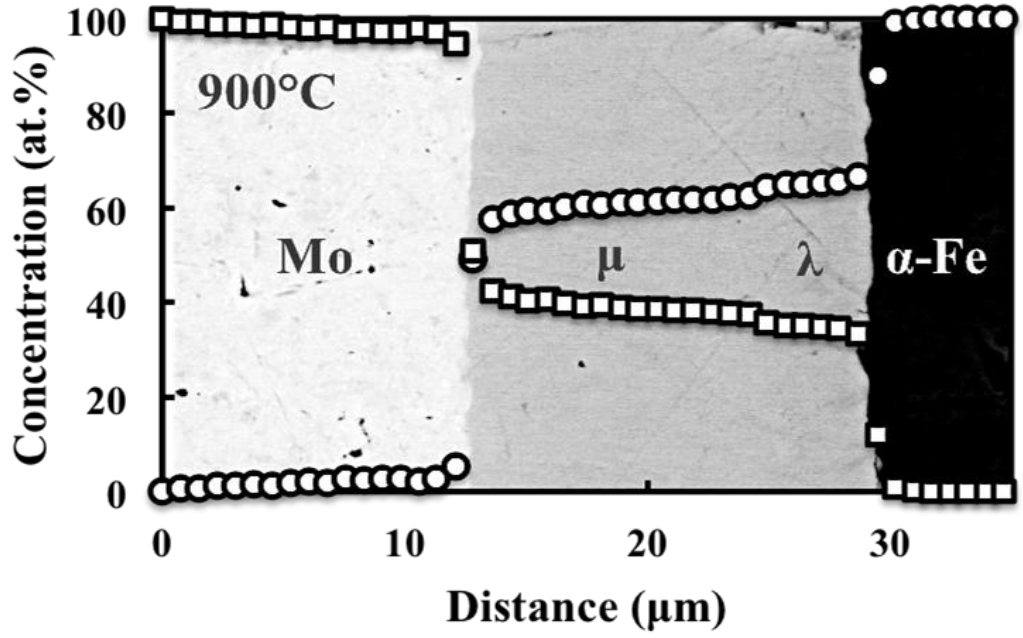

Figure 34: BSE micrograph and superimposed concentration profile of Fe vs. Mo diffusion couple annealed at 900°C for 30 days.

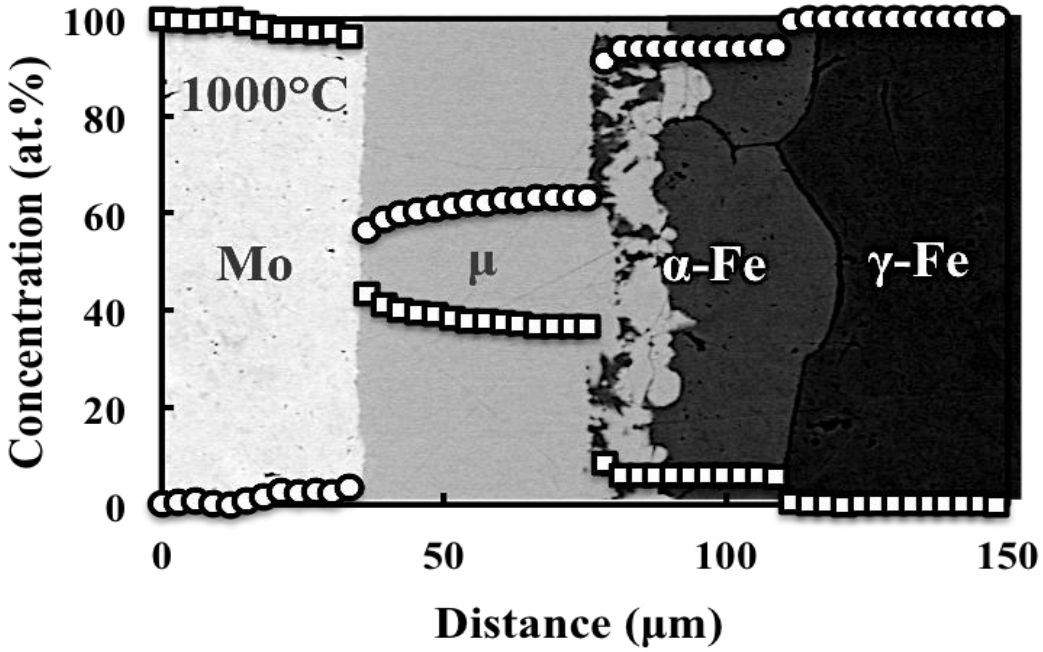

Figure 35: BSE micrograph and superimposed concentration profile of Fe vs. Mo diffusion couple annealed at 1000°C for 15 days.

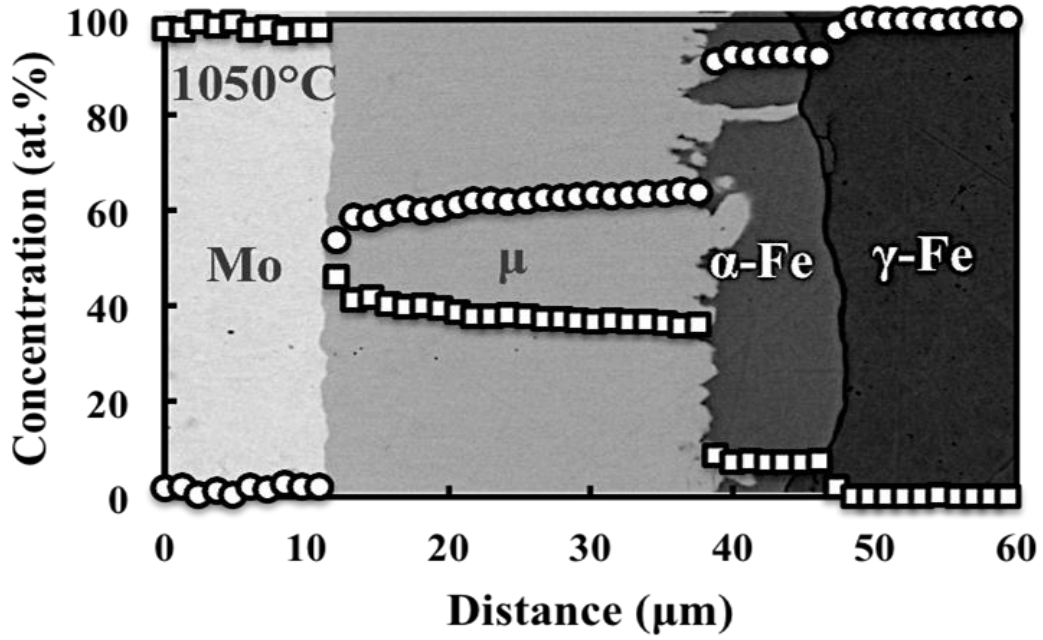

Figure 36: BSE micrograph and superimposed concentration profile of Fe vs. Mo diffusion couple annealed at 1050°C for 3 days.

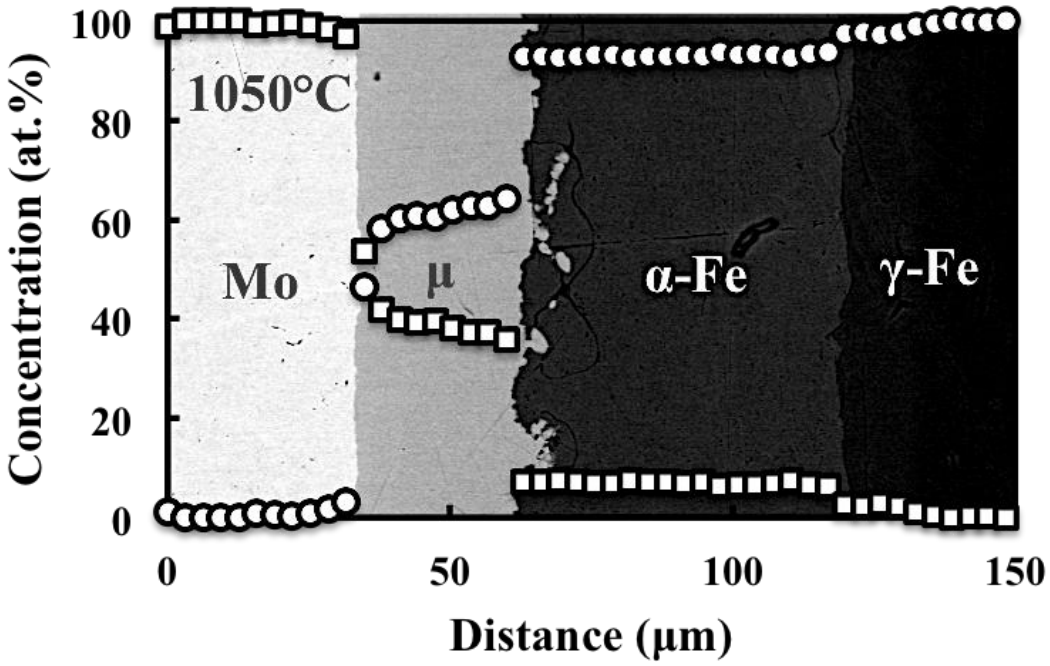

Figure 37: BSE micrograph and superimposed concentration profile of Fe vs. Mo diffusion couple annealed at 1050°C for 5 days.

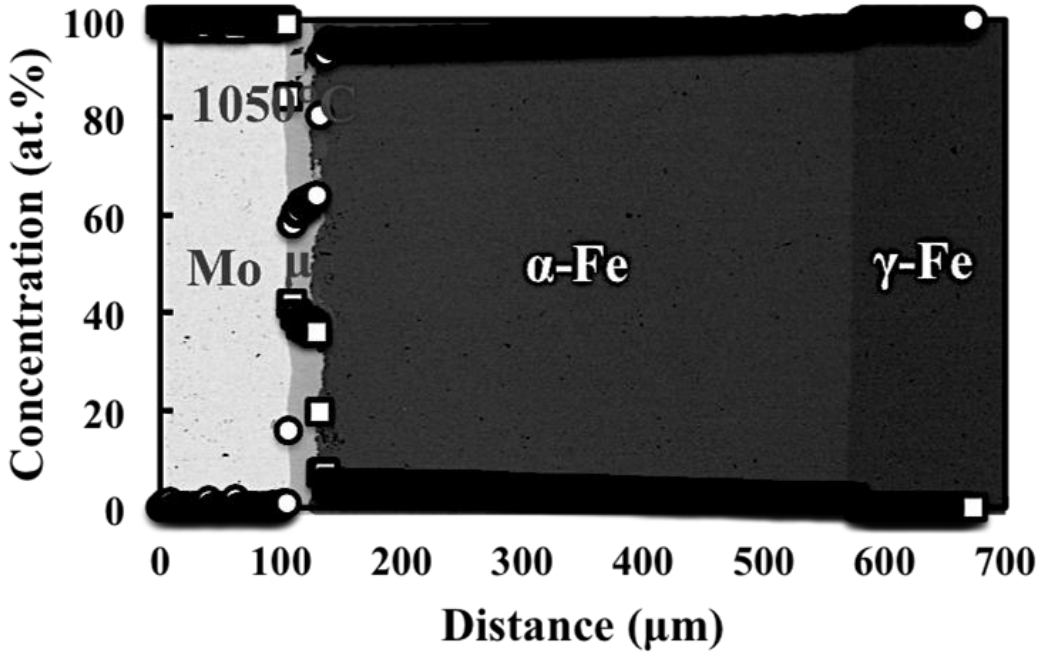

Figure 38: BSE micrograph and superimposed concentration profile of Fe vs. Mo diffusion couple annealed at 1050°C for 8 days.

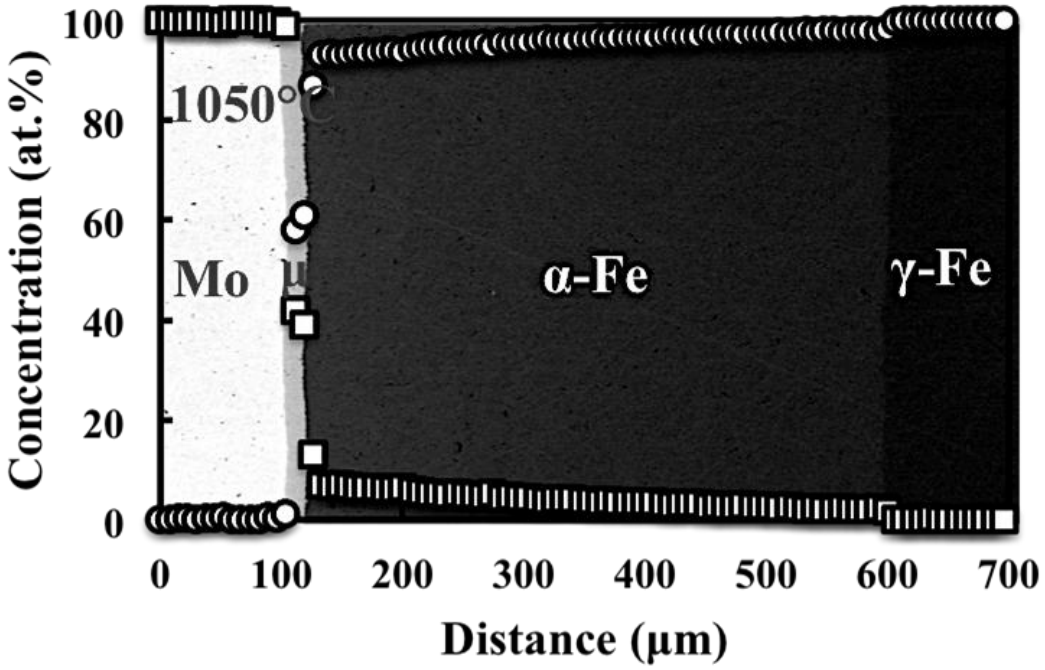

Figure 39: BSE micrograph and superimposed concentration profile of Fe vs. Mo diffusion couple annealed at 1050°C for 15 days.

4.2.2 Growth Kinetics

Thickness measurements were conducted for the layers observed in each Fe vs. Mo couple and the average values obtained are presented in Table 9. Based on these thickness measurements, parabolic growth constants were calculated for each phase and temperature and are listed in Table 10. An Arrhenius plot of the growth constants calculated for the λ-Fe_2Mo and μ-Fe_7Mo_6 phase layers from 650 to 850°C is shown in Figure 40. The pre-exponential factor and activation energy for growth of the λ-Fe_2Mo and μ-Fe_7Mo_6 phases were therefore calculated to be 5.9 x 10^{-5} m^2/s and 234 kJ/mole and 1.2 x 10^{-9} m^2/s and 154 kJ/mole, respectively. Because the μ-Fe_7Mo_6 phase was the consistent phase at each anneal temperature, an Arrhenius plot of the growth constants throughout the entire temperature range is shown in Figure 41. This plot shows that there is a different trend for the couples annealed at higher temperatures, 900 to

1050°C, than those annealed at lower temperatures, 650 to 850°C. Again, the pre-exponential factor and activation energy for growth of the μ-Fe_7Mo_6 phase in the lower temperature range were calculated to be approximately 1.2 x 10^{-9} m^2/s and 154 kJ/mole, respectively, while in the higher temperature range they were not determined due to the fact that the growth constants calculated for the couples annealed at 1050°C do not overlap. Based on the thickness values calculated for the series of diffusion couples annealed at 1050°C for various times, the growth rates of the μ-Fe_7Mo_6 and the α-Fe layers do not appear to be parabolic in nature, as shown in Figure 42 where the thickness is plotted as a function of the square root of the anneal time. This result suggests that the growth of these phases in this temperature range is not diffusion controlled.

Table 9: Average thickness measurements for different phases observed in Fe vs. Mo diffusion couples.

Temp. (°C)	**Time (days)**	**λ (μm)**	**μ (μm)**	**α (μm)**
650	60	0.9	0.6	N.A.
750	30	1.3	1.0	N.A.
850	15	5.4	1.5	N.A.
850	30	5.7	2.0	N.A.
900	15	4.0	11.0	N.A.
1000	15	N.A.	23.3	20.8
1050	3	N.A.	24.4	7.3
1050	5	N.A.	25.4	52.4
1050	8	N.A.	23.0	431.0
1050	15	N.A.	16.6	457.5

Table 10: Calculated parabolic growth constants for different phases observed in Fe vs. Mo diffusion couples.

Temp. (°C)	Time (days)	λ (m^2/s)	μ (m^2/s)	α (m^2/s)
650	60	3.9×10^{-18}	2.2×10^{-18}	N.A.
750	30	4.2×10^{-17}	1.8×10^{-17}	N.A.
850	15	6.3×10^{-16}	8.6×10^{-17}	N.A.
850	30	1.1×10^{-15}	7.4×10^{-17}	N.A.
900	15	6.2×10^{-16}	4.7×10^{-15}	N.A.
1000	15	N.A.	2.1×10^{-14}	1.7×10^{-14}
1050	3	N.A.	1.2×10^{-13}	1.0×10^{-14}
1050	5	N.A.	8.9×10^{-14}	3.2×10^{-13}
1050	8	N.A.	3.8×10^{-14}	1.3×10^{-11}
1050	15	N.A.	1.1×10^{-14}	8.1×10^{-12}

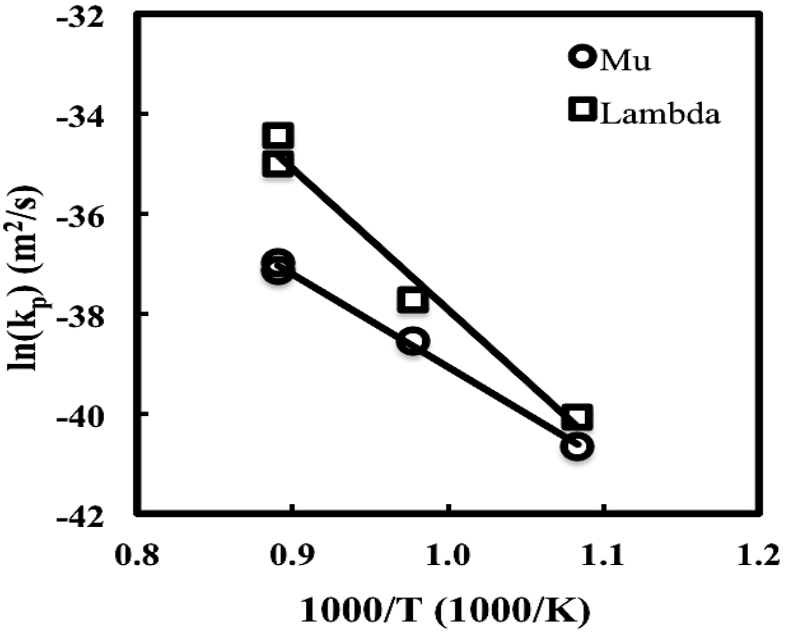

Figure 40: Arrhenius plot of parabolic growth constants calculated for λ-Fe_2Mo and μ-Fe_7Mo_6 from low temperature (650 to 850°C) diffusion couples.

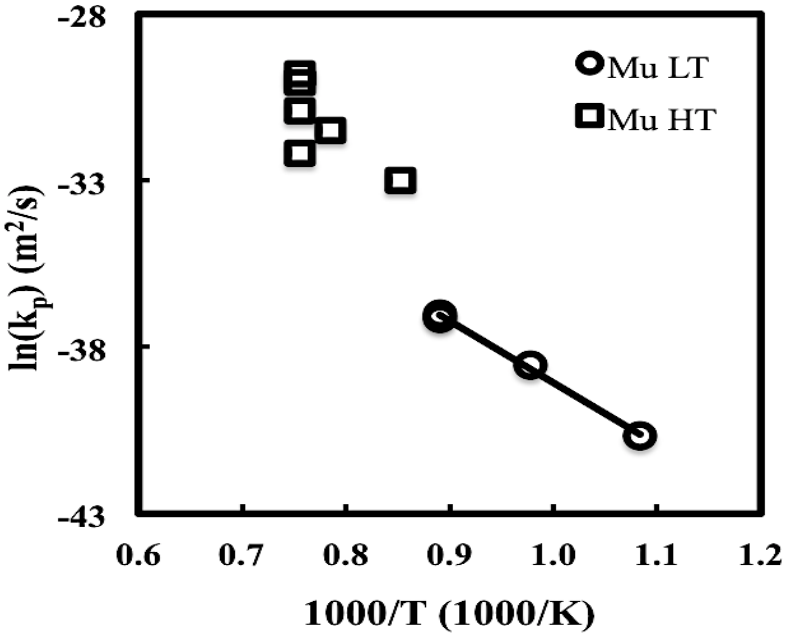

Figure 41: Arrhenius plot of parabolic growth constants calculated for μ-Fe_7Mo_6 from low temperature (650 to 850°C) and high temperature (900 to 1050°C) diffusion couples.

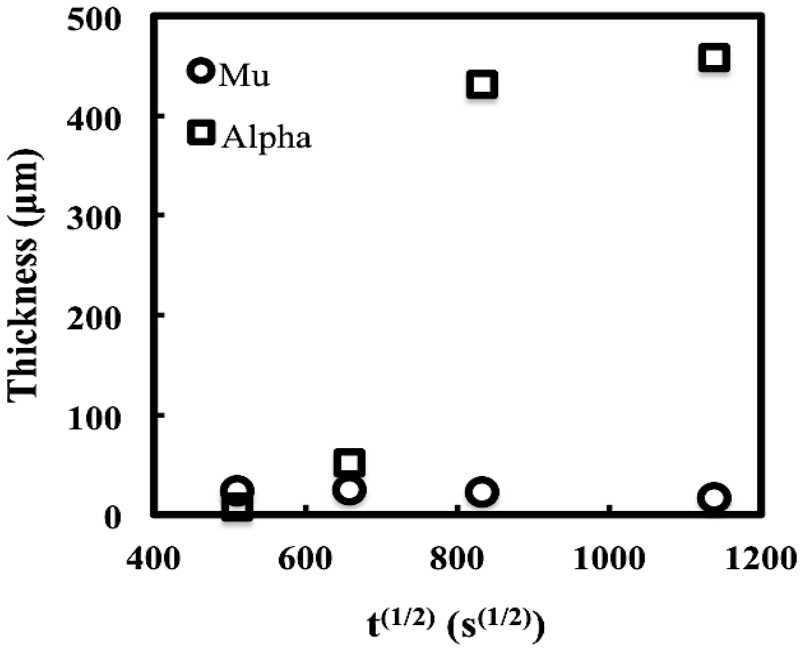

Figure 42: Plot of thickness vs. square root of time for Fe vs. Mo couples annealed at 1050°C indicating that the growth of the μ-Fe_7Mo_6 and α-Fe phases is not parabolic in nature.

4.3 Fe vs. Zr Diffusion Couples

Several diffusion couples were assembled between Fe and Zr and were annealed at the temperatures and times listed in Table 11. The binary Fe-Zr phase diagram is also repeated here in Figure 43 with dotted lines indicating the anneal temperatures. Some important features of the phase diagram are the slight solubility of Fe in Zr between 795 and 940°C and the negligible solubility of Zr in Fe and Fe in Zr at temperatures below 795°C, the existence of four intermediate phases, $FeZr_3$, $FeZr_2$, Fe_2Zr , and $Fe_{23}Zr_6$, and the allotropic transformations of both Fe and Zr from bcc to fcc at 912°C and from hcp to bcc at 863°C, respectively. The anneal temperatures were specifically chosen to investigate the effect of the allotropic transformations of Fe and Zr on the interdiffusion behavior between them. The times were determined based on preliminary results of the higher temperature couples.

Table 11: Experimental diffusion couple matrix for the Fe-Zr system.

Diffusion Couple		**Temperature (°C)**	**Anneal Time (days)**
Side 1	**Side 2**		
Fe	Zr	750	30
Fe	Zr	850	15

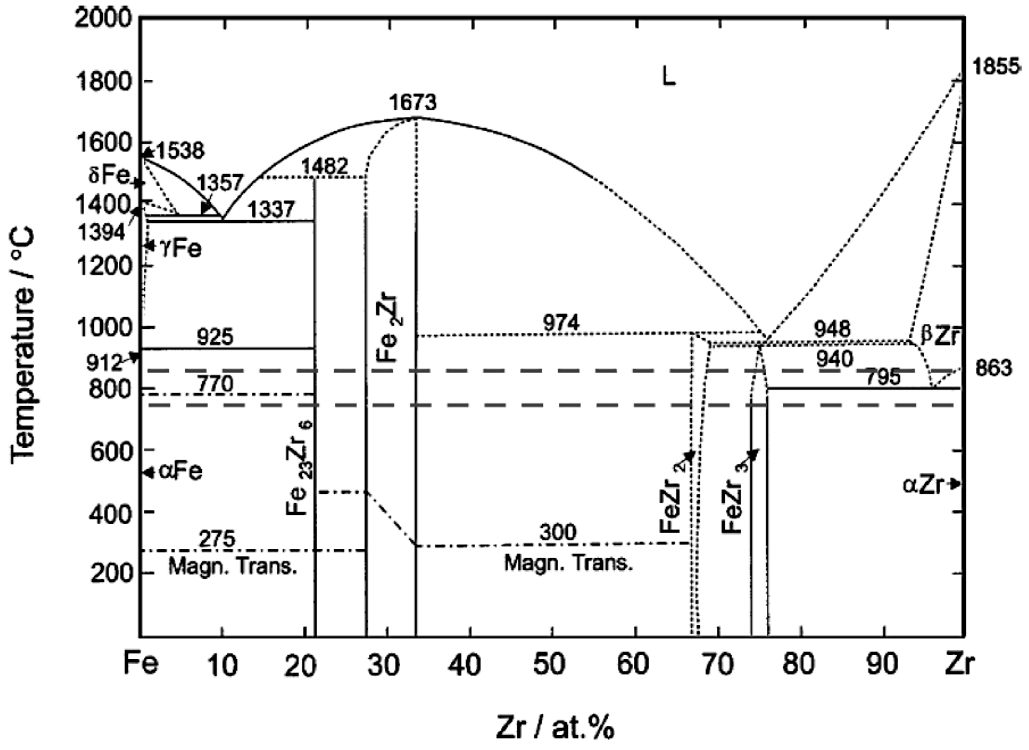

Figure 43: Binary Fe-Zr phase diagram with dotted lines representing anneal temperatures.

4.3.1 Interdiffusion Zone Microstructure

Typical backscatter electron micrographs of the interdiffusion zones that developed in each of the Fe vs. Zr diffusion couples are presented in Figure 44 through Figure 45. The corresponding concentration profiles are superimposed on each micrograph for clarity. In the couple annealed at 750°C for 30 days, two intermetallic phases were observed and were identified as $FeZr_3$ and $FeZr_2$ based on compositional data obtained via EDS and the binary phase diagram. In the couple annealed at 850°C, however, there were also two intermetallic layers present, but they were identified via EDS and the phase diagram as Fe_2Zr and $Fe_{23}Zr_6$. Therefore, all four intermetallics presented on the phase diagram were observed, but only two appeared to develop in each couple.

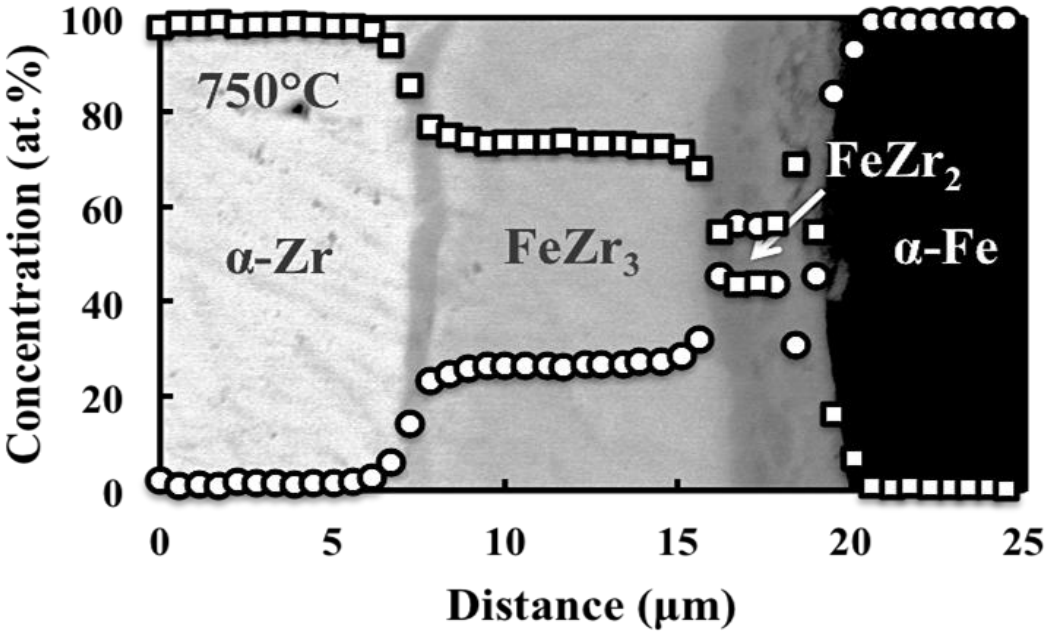

Figure 44: BSE micrograph and superimposed concentration profile of Fe vs. Zr diffusion couple annealed at 750°C for 30 days.

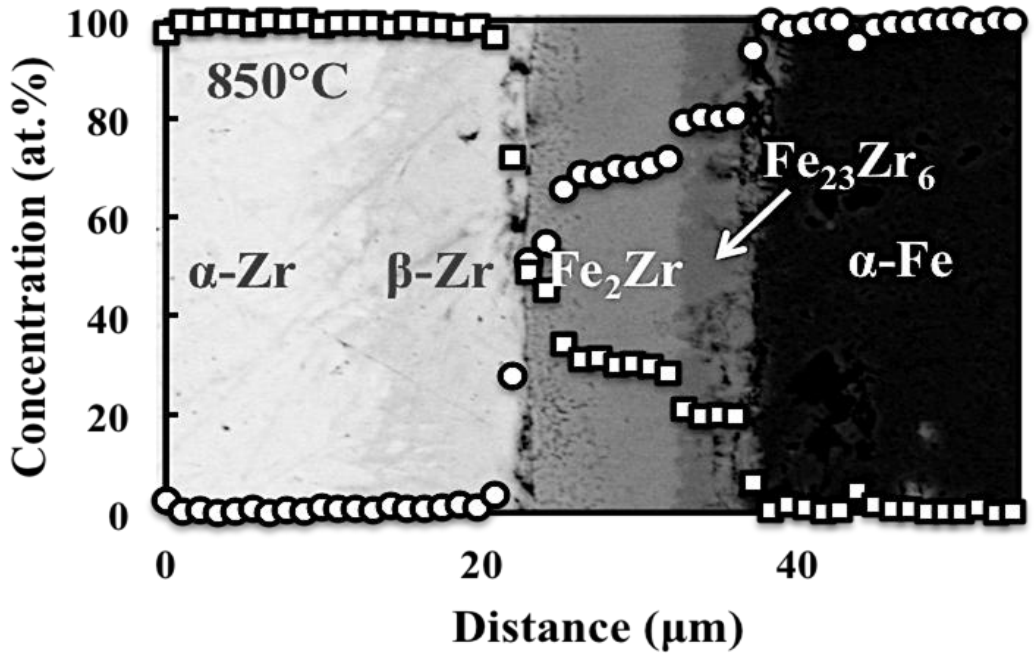

Figure 45: BSE micrograph and superimposed concentration profile of Fe vs. Zr diffusion couple annealed at 850°C for 15 days.

CHAPTER 5: DISCUSSION

5.1 Mo vs. Zr Diffusion Couples

The results obtained through this investigation regarding the Mo-Zr system were compared with those reported in literature. All of the phase diagrams presented show Mo_2Zr as the only intermediate phase that exists in this system. In the earlier diffusion studies conducted in 1964 and 1987, this intermetallic was not observed [33, 34]. However, while it is not obvious at first, a thin layer of Mo_2Zr did form in each of the Mo vs. Zr diffusion couples analyzed in this study. The thickness of this Mo_2Zr layer is very small relative to the Zr solid solution phase that formed in the remainder of the interdiffusion zone and hence could have been indistinguishable at the time the previous studies were conducted. In general, the concentration profiles presented for the high temperature couples characterized in this study agree well with the results of Karpinos who reported one-sided diffusion of Mo into Zr with increasing Mo solubility with increasing anneal temperature and no diffusion of Zr into Mo [34].

The growth kinetics of the Mo_2Zr phase was also considered in this investigation. Based on the Arrhenius plot presented in Figure 26 the pre-exponential factor and activation energy for growth were calculated to be 6.5×10^{-15} m^2/s and 90 kJ/mole, respectively. However, the parabolic growth constant calculated for the Mo_2Zr layer that developed in the couple annealed at 700°C is higher than the value predicted by the trend line. This suggests that the change from β-Zr to α-Zr as the phase neighboring the Mo_2Zr intermetallic layer influences its growth rate. Possible explanations for this difference will be presented later in this section as the microstructure of the interdiffusion zone that developed in the couple annealed at 700°C will be further discussed.

Concentration dependent interdiffusion coefficients were calculated for the Zr solid solution layer that developed in the couples annealed at 850°C and above. As shown in Figure 27, the interdiffusion coefficients decrease exponentially with an increase in Mo concentration. Based on the values calculated at 6 at. % Mo for each temperature, the interdiffusion coefficients obey the Arrhenius relationship as shown in Figure 27. This plot was used to determine the pre-exponential factor and activation energy to be approximately 3.8 x 10^{-8} m^2/s and 150 kJ/mole, respectively. At 1050°C, the interdiffusion coefficient in the Zr solid solution phase was calculated to range from 6.4 x 10^{-14} m^2/s at 2 at. % Mo to 2.8 x 10^{-14} m^2/s at 11 at. % Mo. According to the study presented by Bhatt in 2000, the composition dependent interdiffusion coefficient for the Mo solid solution phase at 2358K (2085°C) was calculated to range from 1.63 x 10^{-13} to 1.27 x 10^{-14} m^2/s for Zr concentrations from 4.9 to 0 at.% respectively [29]. Therefore, the values presented by Bhatt for the Mo solid solution phase at 2085°C are around the same magnitude as those calculated in this study for the Zr solid solution phase at 1050°C.

The interdiffusion coefficient for the Mo_2Zr intermediate phase at 2093K (1820°C) was also calculated by Bhatt and was determined to be 8.83 x 10^{-14} m^2/s. Again the value of the interdiffusion coefficient in this phase at 1820°C is approximately the same as that calculated for the Zr solid solution phase at 1050°C. This suggests that the interdiffusion coefficient for the Zr solid solution phase would be significantly higher than for either the Mo solid solution or Mo_2Zr phases at any given temperature. Also, the homogeneity range of the Zr solid solution phase is much larger than that of the other two phases. These two facts support the formation of a large Zr solid solution layer in the interdiffusion zone of these couples with negligible layers of both Mo solid solution and Mo_2Zr. Another factor that could influence the growth kinetics and inhibit the

formation of the Mo_2Zr layer is that the crystal structure is a complex cubic structure that requires ordering and is more difficult to arrange as compared to simply mixing two bcc materials into a solid solution phase.

Another aspect of the Mo-Zr system that was investigated via the diffusion zone characterization was the homogeneity range of each of the three phases present on the phase diagram. Based on the concentration profiles for each of the couples, there is negligible solubility of Zr in Mo. Also, because the thicknesses of the Mo_2Zr layers were so low, an accurate measurement of solubility within this phase could not be performed. Therefore, only the solubility of Mo in Zr was considered in this study. A schematic of the Zr-rich segment of the Mo-Zr binary phase diagram was developed based on the compositional data obtained from the interdiffusion zones that developed in each of the couples and is presented in Figure 46.

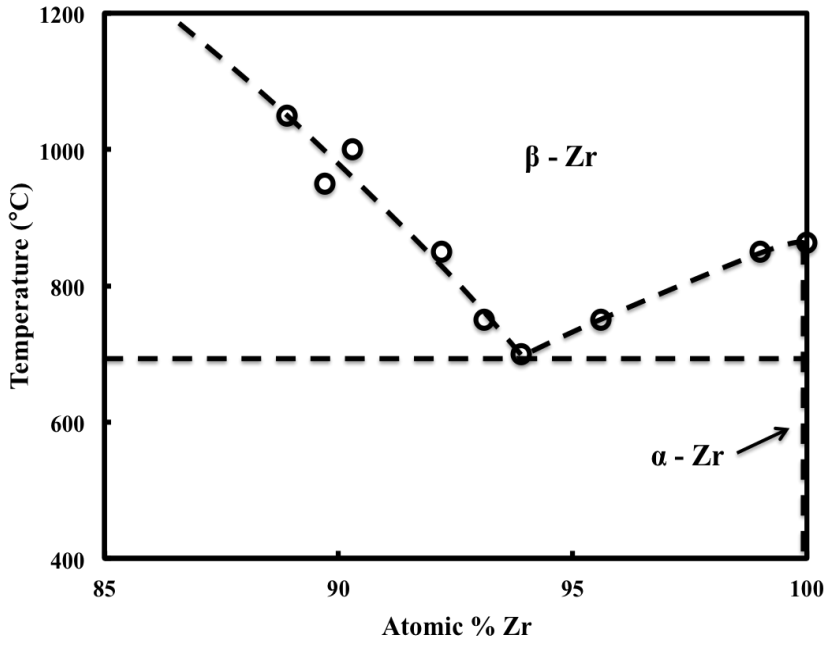

Figure 46: Schematic of Zr-rich segment of Mo-Zr binary phase diagram where open circles represent compositional data points obtained from interdiffusion zones in the Mo vs. Zr diffusion couples characterized in this study and dotted lines indicate suggested phase region boundaries.

The schematic of this portion of the phase diagram agrees most closely with the phase diagram presented by Zinkevich, as shown in Figure 8a, that was developed based on a thermodynamic assessment [30, 31]. The solubility limits according to this work and Zinkevich's assessment match relatively well at each temperature, with the exception of 700°C, and are significantly lower than those reported in the phase diagrams suggested by other authors. As mentioned previously, the couple annealed at 700°C had a layer in the interdiffusion zone with a constant composition of approximately 6 at. % as shown in Figure 20. Based on the results of this work and the schematic phase diagram presented in Figure 46, it appears that the β-Zr → α-Zr + Mo_2Zr eutectoid reaction temperature is near 700°C rather than at 738°C as suggested by the phase diagram presented in Figure 7. There has been some discrepancy between the reported values for both the eutectoid temperature and composition. Table 12 lists the values reported in literature regarding this reaction.

Table 12: Values reported for β-Zr → α-Zr + Mo_2Zr eutectoid reaction temperature and composition according to various authors.

Author	**C_e (at. % Zr)**	**T_e (K)**	**T_e (°C)**	**Reference**
Domagala	92.5 ± 1.0	1053 ± 5	780 ± 5	[50]
Svechnikov	92.0	1053 ± 5	780 ± 5	[51]
Rudy	92.8	903	630	[52]
Samsonor	-	1011 ± 30	738 ± 30	[53]
Brewer	92.8 ± 1.0	1011 ± 30	738 ± 30	[28]
Zinkevich	93.7	1003	730	[30, 31]
Perez	95.7	1050	777	[32]
This Study	93.9 ± 0.4	~ 973	~ 700	[This Study]

As shown in the table, the eutectoid temperature has been reported to be anywhere from as high as 780°C by Domagala to as low as 630°C by Svenhnikov. The eutectoid compositions reported also have a relatively wide range from 92.0 to 95.7 atomic % Zr. The values found in this study lie near the middle of both of these ranges. Again, the data observed in this work most closely agrees with the values recently reported by Zinkevich in a thermodynamic assessment of the Mo-Zr system. However, the eutectoid temperature suggested here is still slightly lower than that proposed by Zinkevich.

According to the original Mo-Zr phase diagram presented in Figure 7, only a Mo_2Zr layer should have formed in the interdiffusion zone of a Mo vs. Zr diffusion couple isothermally annealed at 700°C. If, instead, the eutectoid temperature is indeed lower than initially thought based on the phase diagrams, the additional layer present in the interdiffusion zone of the 700°C couple would be a β-Zr layer as observed in the remainder of the couples. If this is the case, then the explanation for the Mo_2Zr growth constant being higher than expected based on the Arrhenius trend followed by the Mo_2Zr layers that developed in the rest of the couples is not valid. The boundary condition would not be changed because the layer adjacent to the Mo_2Zr layer would still be β-Zr and not α-Zr. However, the thickness of this β-Zr layer should be higher based on the anneal time and the diffusion coefficient extrapolated from the pre-exponential factor and activation energy calculated from the high temperature diffusion couples. Therefore, it seems that reducing the anneal temperature still affects the growth kinetics of both the Mo_2Zr and Zr solid solution layers that develop in the interdiffusion zone. The significantly reduced solubility of Mo in the β-Zr layer at this temperature could influence the growth rates of these phases by reducing the rate at which the β-Zr layer can develop and consequently increasing the relative rate that the Mo_2Zr layer forms.

5.2 Fe vs. Mo Diffusion Couples

The results obtained through this investigation regarding the Fe-Mo system were compared with those reported in literature. Two main aspects of the phase diagram can be commented on based on this work which are the existence of the λ phase and the homogeneity range of the μ. Based on early reports of the phase diagram, the λ phase was not included because most investigators up to that point had not observed it [26]. In 1967, Sinha redrew the phase diagram to include this phase, as shown in Figure 10a, because it had been experimentally observed several times since [36]. However, Heijwegen conducted a diffusion couple analysis in 1974 and again did not observe the λ phase and consequently removed it from the phase diagram as shown in Figure 10b [37]. Based on more recent thermodynamic assessments of the system conducted by both Guillermet and Zinkevich, the λ phase does exist as an intermediate phase on the equilibrium phase diagram [31, 38]. Both phase diagrams presented by Guillermet and Zinkevich agree rather well with the exception of some slight differences in homogeneity ranges. In this study, the λ phase was observed in the interdiffusion zone of the couples annealed at or below 900°C as expected as the λ phase is only stable up to 927°C based on the phase diagram shown in Figure 9. Because there is not a large composition difference between the λ and the μ phases, there is very little contrast difference and the formation of the two distinct layers is not easily observed. This is particularly true of the higher temperature anneals where the higher solubility of the μ phase makes the composition difference between the two even smaller and harder to distinguish. However, based on the BSE micrographs and corresponding concentration profiles, it is clear that both phases are present in the interdiffusion zone as distinct layers in the couples annealed at or below 900°C.

The concentration profiles for several of the diffusion couples show a significant composition range over several percent in the μ phase which agrees well with the phase diagram presented by Guillermet. More interestingly, however, based on a few of the concentration profiles for the couples annealed at the lower temperatures where the λ phase is stable, it too appears to have a homogeneity range of at least a few percent as shown in Figure 32 through Figure 34. This indicates that the λ phase should not be represented as a line compound as it is currently in the phase diagram and should instead have a slight range of composition.

Based on the thickness measurements of the intermetallic layers in the couples annealed at and below 850°C, an Arrhenius trend for both the λ and μ phases was plotted as shown in Figure 40. The pre-exponential factors and activation energies for growth of the λ-Fe_2Mo and μ-Fe_7Mo_6 phases were therefore calculated to be 5.9 x 10^{-5} m^2/s and 234 kJ/mole and 1.2 x 10^{-9} m^2/s and 154 kJ/mole, respectively. Because the μ-Fe_7Mo_6 phase was the consistent phase at each anneal temperature, an Arrhenius plot of the growth constants throughout the entire temperature range is shown in Figure 41. This plot shows that there is a different trend for the couples annealed at higher temperatures, 900 to 1050°C, than those annealed at lower temperatures, 650 to 850°C. In the higher temperature range the pre-exponential factor and activation energy for growth of the μ phase were not determined due to the fact that the growth constants calculated for the couples annealed at 1050°C do not overlap. Based on the thickness values calculated for the series of diffusion couples annealed at 1050°C for various times, the growth rates of the μ-Fe_7Mo_6 and the α-Fe layers do not appear to be parabolic in nature, as shown in Figure 42 where the thickness is plotted as a function of the square root of the anneal time. This result suggests that the growth of these phases in this temperature range is not

diffusion controlled and is instead interface or reaction controlled. However, in the low temperature range, two couples were annealed at 850°C for different times, 15 and 30 days. As shown in Figure 40 the two data points corresponding to these couples overlap relatively well suggesting that at low temperatures the formation of these layers is diffusion controlled. At lower temperatures, diffusion is slower and hence might be the rate limiting factor while at high temperatures, with diffusion occurring much more rapidly, the supply rate of atoms to the interface may be higher than the rate at which the reaction can occur causing the process to be interface or reaction controlled in this temperature regime. Based on the plot shown in Figure 42, the growth of the α-Fe phase appears to be asymptotic in nature while the μ layer seems to grow to a critical thickness and remain constant or may even deplete over time. Cases have been reported by Dybkov in which reaction diffusion in binary systems causes situations where a minimal thickness of a layer must form in order for another layer to start to develop or non-linear and asymptotic growth of certain phases occurs [7].

Another feature of the interdiffusion zone microstructures that developed in the two couples annealed at 850°C, was the additional layer with approximately 4 at. % Mo that was not expected to form based on the phase diagram. This additional layer with relatively constant composition may be explained by the magnetic transition of Fe from ferromagnetic to paramagnetic at 769°C. It has been reported by Miodownik that one of the most prominent effects of magnetic transformations on phase boundaries is a change in terminal solubility limits created by the intersection of a transus line and a Curie temperature [54]. This shift in solubility due to the magnetic transition could possibly account for the formation of this layer as these two couples were annealed above the Curie temperature. However, a further investigation would need to be conducted in order to verify this.

5.3 Fe vs. Zr Diffusion Couples

The Fe-Zr system has been studied extensively, but there are still uncertainties regarding the existence and temperature/composition ranges of the intermetallic compounds present in the phase diagram. Contradictory results have been published concerning the existence of the phase $Fe_{23}Zr_6$ (or Fe_3Zr as denoted in earlier works). Several authors experimentally observed this phase in cast alloys of varying compositions. However, Stein suggested that this is an oxygen stabilized phase that does not belong to the binary diagram. There have also been some controversies over the homogeneity ranges of the Fe_2Zr and $FeZr_3$ phases. Consequently, some experimental and thermodynamic assessments of the binary Fe-Zr system have been conducted in an attempt to clarify these discrepancies and have resulted in several variations of the equilibrium phase diagram as repeated in Figure 47 for reference.

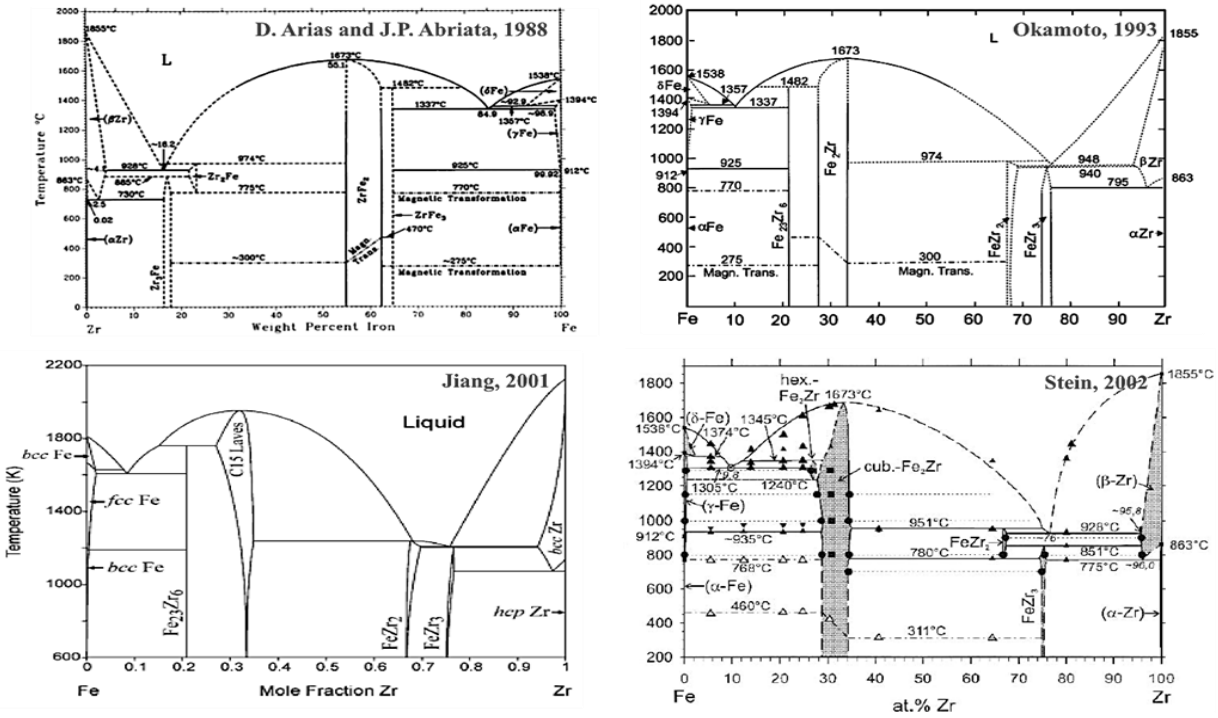

Figure 47: Various versions of the Fe-Zr phase diagram based on thermodynamic calculations and experimental values.

The results obtained from the characterization of the two diffusion couples analyzed in this system will be discussed with respect to each of these issues concerning the phase diagram. Based on the compositional analysis performed, the intermetallic layers in the Fe vs. Zr couple annealed at 750°C were identified as $FeZr_2$ and $FeZr_3$ while in the couple annealed at 850°C the intermetallic layers were identified as Fe_2Zr and $Fe_{23}Zr_6$. A schematic of the layers that developed in each couple is presented in Figure 48 along with the corresponding phases circled on one of the phase diagrams for clarity. Based on these results, it appears that the change in the boundary condition from α to β-Zr alters the intermetallic layers that develop in the interdiffusion zone. One possible explanation for this change is that upon transformation to β-Zr there is a larger solubility for Fe and the more Fe-rich intermetallics can form while α-Zr has a negligible solubility and the more Zr-rich phases form instead. However, the transformation from ferromagnetic to paramagnetic Fe at 769°C could have an influence on the diffusion behavior in this system also and could possibly affect intermetallic formation as it has been reported that the magnetic transformation changes ordered phase stability in the Fe-Ni system [54].

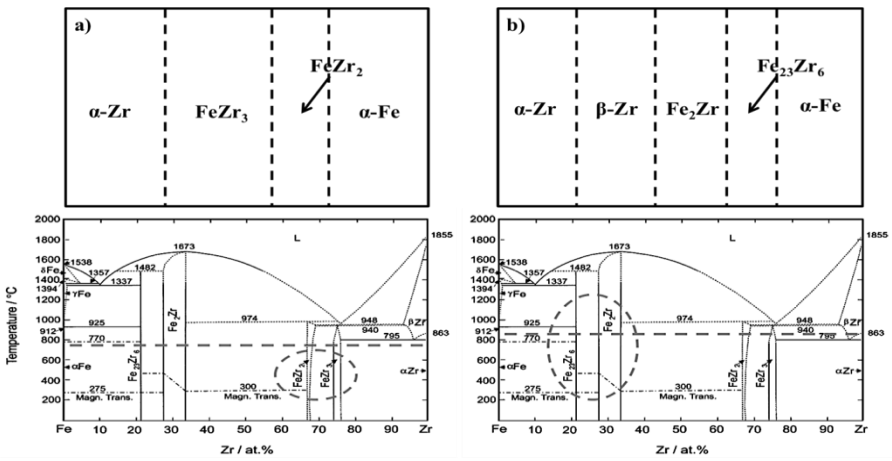

Figure 48: Schematic representations of and corresponding phases diagrams showing phases that developed in the interdiffusion zones of Fe vs. Zr couples annealed at a) 750°C and b) 850°C.

One of the main controversies regarding this system is the existence and stability of the $Fe_{23}Zr_6$ phase. Based on compositional analysis, this phase formed a layer approximately 5 μm in thickness in the Fe vs. Zr couple annealed at 850°C. According to Stein, this phase is stabilized by oxygen and is not part of the equilibrium binary Fe-Zr system. A BSE micrograph of one of the alloys in which Stein observed the $Fe_{23}Zr_6$ phase is shown in Figure 49a. A BSE micrograph of the interdiffusion zone that formed in the couple annealed at 850°C is shown in Figure 49b. The corresponding oxygen maps are shown in Figure 49c and Figure 49d respectively. In Figure 49c the bright spots indicate increased oxygen levels in the regions corresponding to $Fe_{23}Zr_6$. However, in Figure 49, the dark spots represent increased oxygen content and indicate that the oxygen level in the $Fe_{23}Zr_6$ phase is lower that the impurity content in the pure Fe suggesting that the $Fe_{23}Zr_6$ phase is not necessarily oxygen stabilized.

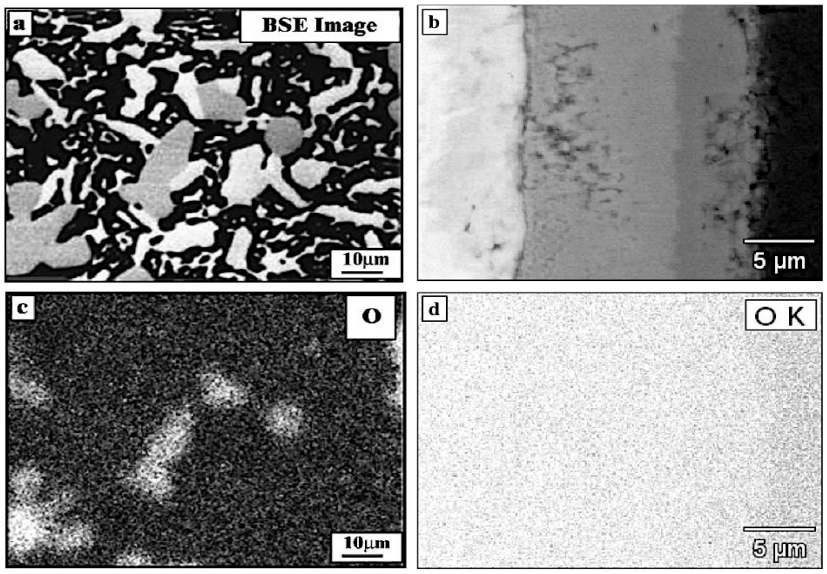

Figure 49: a) BSE micrograph of the $Fe_{23}Zr_6$ enriched region of the Fe-14at.%Zr alloy heat treated for 100 hours at 1150°C as presented by Stein, b) BSE micrograph of Fe vs. Zr diffusion couple annealed for 15 days at 850°C as presented in this study, c) oxygen map with bright spots representing increased oxygen content in the $Fe_{23}Zr_6$ regions, and d) oxygen map with gray spots representing increased oxygen content.

Another point of contention regarding the various phase diagrams presented for the Fe-Zr system are the homogeneity ranges of the various intermetallic phases. Several authors showed limited or no solubility in the Fe_2Zr and $FeZr_3$ phases. However, some indicated that the composition of these phases ranges over several percent. The concentration profiles collected from the diffusion couples annealed at 750 and 850°C suggest that there is some solubility within both of these phases. The couple annealed at 750°C developed an $FeZr_3$ layer with approximately 6 at. % variation in composition and the couple annealed at 850°C developed an Fe_2Zr layer with approximately 3 at. % variation in composition as shown in Figure 50. These results combined with the other observations made based on the two couples characterized in the Fe-Zr system suggest that the phase diagram proposed by Okamoto is the most appropriate for this system.

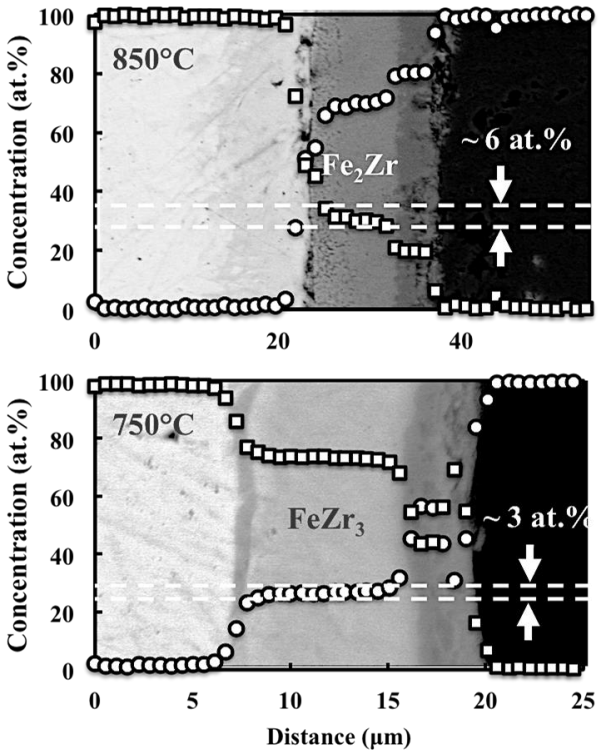

Figure 50: BSE micrographs and superimposed concentration profiles showing homogeneity ranges of Fe_2Zr and $FeZr_3$ phases.

5.4 General Discussion

The results of this work indicate that the allotropic transformations of both Fe and Zr play a role in the interdiffusion behavior of these systems. It appears that both the phase formation and growth rates are affected by the phase transformations of the terminal ends of the diffusion couples. It seems to make sense that a change in crystal structure would be accompanied by a change in interdiffusion behavior since the similarity in crystal structures between two phases is known to influence the growth rates of intermediate phases. However, the exact effects of allotropic transformations on interdiffusion behavior remain unclear.

A related study has recently been conducted to investigate the interdiffusion behavior between pure depleted uranium and iron [55]. In this study, mechanically bonded diffusion couples were also used to analyze the phase formation and growth kinetics of the intermediate phases in the U-Fe system. Diffusion anneal temperatures of 580, 615, 650, 680, and 700°C were chosen to be both above and below the allotropic transformation from orthorhombic α to tetragonal β-U. Both of the intermetallic phases present on the binary phase diagram, U_6Fe and UFe_2, appeared in the interdiffusion zone. Based on the corresponding concentration profiles, parabolic growth constants and integrated interdiffusion coefficients were calculated. Figure 51 shows an Arrhenius plot of the integrated interdiffusion coefficients. From this plot the pre-exponential factors and activation energies of diffusion for both the U_6Fe and UFe_2 phases were calculated. As shown in the figure, a discontinuity in the Arrhenius trend line for each intermediate phase was observed near the allotropic transformation temperature of U at 667°C. This suggests that the allotropic transformation of uranium affected the interdiffusion behavior of these two intermetallics.

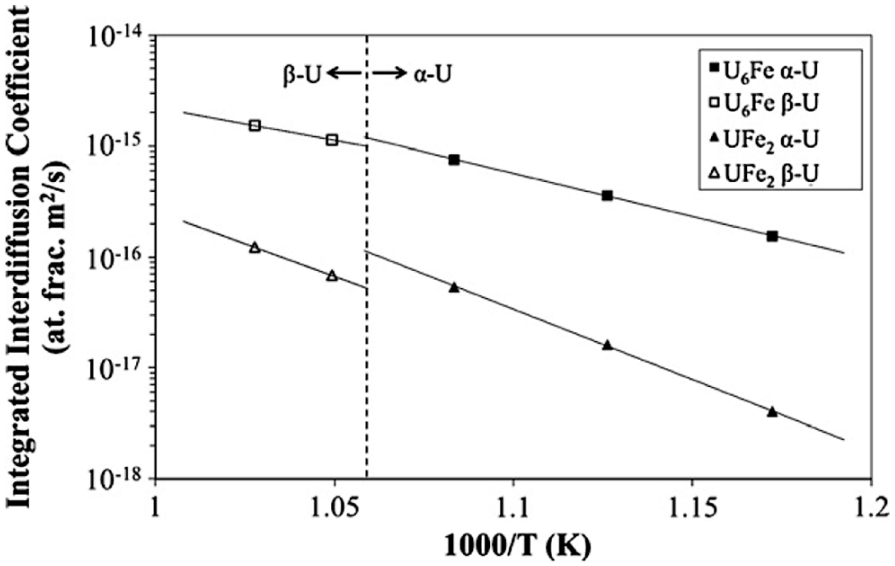

Figure 51: Arrhenius plot of integrated interdiffusion coefficients for both U_6Fe and UFe_2.

While Fe was also involved in this system, the diffusion anneal temperatures used in this study were well below either the allotropic or magnetic transformation temperatures of Fe. Therefore, this discontinuity of the integrated interdiffusion coefficients should solely be due to the transformation of uranium. As previously mentioned, in order for an allotropic transformation to exist, the free energy curves of the two phases must intersect, which corresponds to a difference in heat capacity of the two phases. Therefore, a change in the temperature dependence of the thermodynamic driving force for the reaction to occur can be expected upon the allotropic transformation. In addition, the crystal structure and corresponding binding energies are altered by the transformation and can affect the distance and consequently the rate at which the atoms diffuse.

The aforementioned factors may explain some of the reasons for the effects of allotropic transformations on the growth rate of certain intermediate phases. However, the results of this work, particularly for the Fe-Zr system, suggest that the allotropic transformation may influence

which intermetallics even develop to an observable thickness in the reaction zone. Because of the difference in temperature and crystal structure upon transformation, different allotropes typically have largely varying solubilities for other elements. As previously discussed, the homogeneity range of a phase and the similarity between adjacent crystal structures are two factors that help to determine which phases form more rapidly. Upon an allotropic transformation, both of these factors can change relatively drastically and hence may consequently promote the formation of different phases. Because the magnetic transition temperature of Fe is in between the two diffusion anneal temperatures used in this work, it is difficult to distinguish the effects of the allotropic and magnetic transformations and hence, the magnetic transition could also play an important role in determining which phases form. Other explanations for such behavior need to be considered upon further study of the system.

It has also been previously observed that many of the transition metals exhibit anomalies in their diffusion behavior [56, 57]. In addition, an important characteristic of the metals showing this anomalous diffusion behavior is that they are all allotropic in nature [58, 59]. Both the diffusion behavior and phase transformation characteristics are correlated to the entropy of fusion [60]. It has been shown by Tiwari that, through this dependence on the entropy of fusion, the diffusion behavior and phase transformation characteristics are related to each other [60]. Again, however, the exact effects of allotropic transformations on the interdiffusion behavior are not completely understood and need to be studied further in order to gain insight into the role that they play in the formation and growth rate of intermediate phases. Additional diffusion experiments should be conducted to better understand the role of the allotropic transformations of Fe and Zr in these systems and then the approach should be extended to study other systems involving allotropic transformations.

CHAPTER 6: SUMMARY AND CONCLUSIONS

6.1 Mo-Zr System

Several diffusion couples were assembled and isothermally annealed at temperatures between 700 and 1050°C for times ranging from 15 to 60 days. In all of the couples a thin layer of the only intermediate phase on the phase diagram, Mo_2Zr, formed. However, this layer was negligible compared to the much larger Zr solid solution layer that developed in each of the diffusion couples. No solubility of Zr into Mo was observed based on the concentration profiles collected from each of the couples. The parabolic growth constants were calculated for the Mo_2Zr layers and were found to obey an Arrhenius relationship excluding that for the couple annealed at 700°C. The corresponding pre-exponential factor and activation energy for the growth of the Mo_2Zr layer were calculated to be 6.5×10^{-15} m^2/s and 90 kJ/mole based on the Arrhenius trend. Using the Boltzmann-Matano method, concentration dependent interdiffusion coefficients were calculated for the Zr solid solution phase based on the couples annealed at 850°C and above. There is a slightly negative exponential dependence of the interdiffusion coefficient on Mo concentration. The interdiffusion coefficients were also found to obey an Arrhenius relationship and the corresponding pre-exponential factor and activation energy were calculated to be 3.8×10^{-8} m^2/s and 150 kJ/mole, respectively. The solubility limits of Mo in Zr were also investigated and the Zr-rich portion of the phase diagram was schematically drawn. This portion of the phase diagram matches Zinkevich's version most closely with respect to the solubility of Mo in Zr in the temperature range investigated in this study. However, the results of this work also suggest that the β-Zr $\rightarrow$ α-Zr + Mo_2Zr eutectoid reaction temperature may be near 700°C, which is slightly lower than most reported values.

6.2 Fe-Mo System

Several diffusion couples were assembled and isothermally annealed at temperatures between 650 and 1050°C for times ranging from 3 to 60 days. In the couples annealed at and below 900°C, both the intermediate phases, λ-Fe_2Mo and μ-Fe_7Mo_6 , present on the binary Fe-Mo phase diagram were observed. The homogeneity range observed in the μ phase agreed well with that suggested in the phase diagram. However, the concentration profiles obtained from these couples indicated that the λ phase is not a line compound and instead exists over a range of a few atomic percent. In the couples annealed above 900°C, only the μ phase and a layer corresponding to α-Fe formed which was the expected result according to the phase diagram. Based on the couples annealed between 650 and 850°C, the pre-exponential factor and activation energy for growth of the λ and μ phases were calculated to be 5.9 x 10^{-5} m^2/s and 234 kJ/mole and 1.2 x 10^{-9} m^2/s and 154 kJ/mole, respectively. Four diffusion couples were annealed at 1050°C for various times to investigate the growth of the μ and α-Fe layers as a function of time. In the higher temperature range the pre-exponential factor and activation energy for growth of the μ phase were not determined due to the fact that the growth constants calculated for the couples annealed at 1050°C do not overlap. This suggests that the growth in this temperature regime does not obey the Arrhenius relationship. Based on the thickness measurements the growth rates of the μ and the α-Fe layers do not appear to be parabolic in nature and hence the growth process is likely reaction controlled rather than diffusion controlled. The formation of an additional layer with an approximately constant composition of 4 at. % Mo in the two couples annealed at 850°C could be due to a change in terminal solubility caused by the magnetic transformation of Fe from ferromagnetic to paramagnetic at 769°C.

6.3 Fe-Zr System

Two diffusion couples between Fe and Zr were assembled and isothermally annealed at 750 and 850°C for 30 and 15 days respectively. Two intermetallic layers developed in the interdiffusion zone of each couple. In the couple annealed at 750°C, the two layers that developed were identified based on compositional analysis as $FeZr_2$ and $FeZr_3$ while the two layers that formed in the 850°C couple were identified as Fe_2Zr and $Fe_{23}Zr_6$. The formation of these four layers accounts for all of the intermediate phases that are known to exist in the binary system, but it is not clear why only two formed in each couple. One possible explanation is the transition of the boundary layer from α to β-Zr alters the intermetallic layers that develop in the interdiffusion zone. The transformation to β-Zr means a larger solubility for Fe and the more Fe-rich intermetallics can form while α-Zr has a negligible solubility for Fe and the more Zr-rich phases form instead. However, the transformation from ferromagnetic to paramagnetic Fe at 770°C could have an influence on the diffusion behavior in this system also and could possibly affect intermetallic formation. Some key features of the phase diagram were also considered based on the results of these two couples. According to Stein, the $Fe_{23}Zr_6$ phase should not be presented on the binary Fe-Zr phase diagram because it is stabilized by oxygen. However, an oxygen map collected from the couple annealed at 850°C did not show increased oxygen content in the $Fe_{23}Zr_6$ layer that developed in the interdiffusion zone and hence does not support the claim that this phase is oxygen stabilized. The homogeneity range of the Fe_2Zr and $FeZr_3$ phases were also determined to be several percent based on the concentration profiles collected from the two diffusion couples. All of the results obtained from the analysis of the diffusion couples indicated that Okamoto's version of the Fe-Zr phase diagram is most appropriate.

CHAPTER 7: FUTURE WORK

In order to conduct a more thorough investigation of the equilibrium phase diagrams and growth kinetics of the various phases that form as a result of interdiffusion in these three systems, several more diffusion couples would need to be annealed and characterized. Also, because all of the phase identifications were based on compositional data and knowledge of the respective binary phase diagrams, TEM should be performed to obtain electron diffraction patters to verify the crystal structures of each of the phases present.

With respect to the Mo-Zr system, various heat treatments should be conducted to investigate the composition and temperature of the β-Zr $\rightarrow$ α-Zr + Mo_2Zr eutectoid reaction. The discrepancy among the growth constant of the Mo_2Zr layer in the couple annealed at 700°C and the Arrhenius trend should then be investigated to determine the reason for the difference. In addition, the homogeneity range and interdiffusion coefficient of the Mo_2Zr phase could be determined and subsequently compared to previous values reported in literature if annealed for a long enough time for the layer to grow substantially larger.

In the Fe-Mo system, further analysis could be done to more accurately determine the homogeneity ranges of the λ-Fe_2Mo and μ-Fe_7Mo_6 phases. Another diffusion couple study should be conducted specifically considering the diffusion behavior as a function of time to better understand the growth kinetics of the phases present and to determine the rate limiting parameters in the different temperature regimes. The effect of the magnetic transformation of ferromagnetic Fe to paramagnetic Fe on the interdiffusion behavior should also be considered further in order to determine the nature of the additional layer that formed in the interdiffusion zone of the couples annealed at 850°C.

Regarding the Fe-Zr system, several more diffusion couples should be characterized in order to draw any firm conclusions with respect to the formation, or lack thereof, of the various intermetallic phases present in the phase diagram. In analyzing these additional couples, a more accurate determination of the homogeneity ranges and stability of these intermediate phases could be made. Particular consideration should be given to investigating the effects of the magnetic transformation of Fe on the formation of certain intermetallics over others. The existence of the $Fe_{23}Zr_6$ phase as an equilibrium phase on the binary phase diagram should also be considered to verify whether or not it is an oxygen stabilized phase.

In general, this study should be extended to further investigate the effects of the allotropic transformations of Fe and Zr on the interdiffusion behavior in these systems. A more systematic approach should be taken to eliminate or better understand the effects of other variables, such as the magnetic transformation of Fe, on the interdiffusion behavior in order to decipher the exact role of the allotropic transformation. This approach could then be extended to investigate the interdiffusion behavior in other systems involving metals that undergo an allotropic transformation to achieve a better understanding of the fundamental reasons for the effects of the transformation.

REFERENCES

[1] DeHoff, R.T., and N. Kulkarni. “The Trouble with Diffusion.” *Materials Research* 5.3 (2002): 209-229. Print.

[2] University of Oslo, “Chapter 5: Solid State Diffusion.” KJM 5120: Defect Chemistry and Reactions (2005). Print.

[3] Van Loo, F.J.J. “Multiphase Diffusion in Binary and Ternary Solid-state Systems.” *Progress in Solid State Chemistry* 20.1 (1990): 47-99. Print.

[4] Philibert, J. “Reactive Diffusion.” *Defect and Diffusion Forum* 66-69 (1990): 995-1014. Print.

[5] Gösele, U., and K.N. Tu. “Growth Kinetics of Planar Binary Diffusion Couples: “Thin-film Case” versus “Bulk Cases”.” *Journal of Applied Physics* 53.4 (1982): 3252-3260. Print.

[6] Dybkov, V. I. “Reaction Diffusion in Heterogeneous Binary Systems Part 3: Multiphase Growth of the Chemical Compound Layers at the Interface between Two Mutually Insoluble Substances.” *Journal of Materials Science* 22 (1987): 4233-4239. Print.

[7] Dybkov, V.I. *Reaction Diffusion and Solid State Chemical Kinetics*. Kyiv: The IPMS Publications (2002). Print.

[8] Kidson, G. “Some Aspects of the Growth of Diffusion Layers in Binary Systems.” *Journal of Nuclear Materials* 3.1 (1961): 21-29. Print.

[9] Kajihara, M. “Analysis of Kinetics of Reactive Diffusion in a Hypothetical Binary System.” *Acta Materialia* 52.5 (2004): 1193-1200. Print.

[10] Kidson, G., and G. Miller. “A Study of the Interdiffusion of Aluminum and Zirconium.” *Journal of Nuclear Materials* 12.1 (1964): 61-69. Print.

[11] Gibbs, G. “Diffusion Layer Growth in a Binary System.” *Journal of Nuclear Materials* 20.3 (1966): 303-306. Print.

[12] Pretorius, R., T. Marais, and C. Theron. “Thin Film Compound Phase Formation Sequence: An Effective Heat of Formation Model.” *Materials Science Reports* 10.1-2 (1993): 1-83. Print.

[13] Fick, A. “On Liquid Diffusion.” *Philosophical Magazine and Journal of Science* 10 (1855): 30-39. Print.

[14] Crank, John. *The Mathematics of Diffusion*. Oxford: Clarendon (1979). Print.

[15] Boltzmann, L. “Zur Integration Der Diffusionsgleichung Bei Variable Diffusionskoeffizienten (Integration of the Diffusion Equation with Variable Diffusion Coefficients).” *Wiedemanns Annalen* 53 (1894): 959. Print.

[16] Matano, C. “On the Relation between the Diffusion Coefficients and Concentrations of Solid Metals (The Nickel-Copper System).” *Japanese Journal of Physics* 8 (1933): 109-113. Print.

[17] Murugan, R. “Phase Transformations in Solids.” (2010): 1-6. Print.

[18] Porter, D.A., Easterling, K.E., and Sherif, M.Y. *Phase Transformations in Metals and Alloys*. Boca Raton, FL: CRC (2009). Print.

[19] Tisza, M. *Physical Metallurgy for Engineers*. Materials Park, OH: ASM International (2001). Print.

[20] Savitskii, E.M. “Polymorphous Metals.” *Metal Science and Heat Treatment* 7.7 (1966): 427-431. Print.

[21] Villars, P., Okamoto, H., and Cenzual, K. “Pure Metal Melting Points and Allotropic Transformations.” *ASM Alloy Phase Diagrams Center*. ASM International (2007). Print.

[22] Grimvall, G., and Ebbsjö, I. “Polymorphism in Metals I.” *Physica Scripta* 12.3 (1975): 168-172. Print.

[23] Zener, C. *Elasticity and Anelasticity of Metals.* Chicago, IL: Chicago University Press (1948). Print.

[24] Grimvall, G. "Polymorphism in Metals II." *Physica Scripta* 12.3 (1975): 173-176. Print.

[25] Massalski, T.B. “Mo-Zr Binary Alloy Phase Diagram as adapted from Zirconium.” *ASM Handbook*: *Alloy Phase Diagrams*. Materials Park, OH: ASM International 3 (1990): 298. Print.

[26] Hansen, M., and K. Anderko. *Constitutions of Binary Alloys*. New York: McGraw Hill (1958). Print.

[27] Kubaschewski, O., and O. von Goldbeck. “Zirconium: Physico-Chemical Properties of Its Compounds and Alloys.” IAEA, Atomic Energy Review, Vienna, Austria, Special Issue No. 6 (1976): 67. Print.

[28] Brewer, L., and R.H. Lamoreaux. “Molybdenum: Physico-Chemical Properties of Its Compounds and Alloys.” IAEA, Atomic Energy Review, Vienna, Austria, Special Issue No. 7 (1980): 344-347. Print.

[29] Bhatt, Y.J., L. Kumar, R.V. Patil, G.B. Kale, and S.P. Garg. “Diffusion Studies in Hf-Mo, Zr-Mo, Cr-Nb, Cr-Ta and Th-Re Systems above 1900K.” *Journal of Alloys and Compounds* 302 (2000): 177-186. Print.

[30] Zinkevich, M., and N. Mattern. “Thermodynamic Assessment of the Mo-Zr System.” *Journal of Phase Equilibria* 23.2 (2002): 156-162. Print.

[31] Zinkevich, M., and N. Mattern. “Thermodynamic Modeling of the Fe-Mo-Zr System.” *Acta Materialia* 50 (2002): 3373-3383. Print.

[32] Perez, R.J., and B. Sundman. “Thermodynamic Assessment of the Mo-Zr Binary Phase Diagram.” *Calphad* 27.3 (2003): 253-262. Print.

[33] Sweeney, W.E., and A.P. Batt. “Electron Probe and X-ray Diffraction Measurements of Intermediate Phases in Zr Diffused with Cr, Fe, Ni, Cu and Mo.” *Journal of Nuclear Materials* 13.1 (1964): 87-91. Print.

[34] Karpinos, D.M., L.R. Vishnyakov, V.P. Moroz, T.N. Bondarenko, and V.P. Dzefanovskii. “Phase Interaction in Composite Materials Zr-Mo, W.” *Powder Metallurgy and Metal Ceramics* 26 (1987): 983-987. Print.

[35] Guillermet, A.F. In Massalski, T.B. *Binary Alloy Phase Diagrams.* 2nd ed. Materials Park: ASM International 2 (1988): 1726-1728. Print.

[36] Sinha, A.K., R.A. Buckley, and W. Hume-Rothery. “Equilibrium Diagram of the Iron-Molybdenum System.” *Journal of the Iron and Steel Institute* 205 (1967): 191-195. Print.

[37] Heijwegen, C., and G. Rieck. “Determination of the Phase Diagram of the Mo-Fe System Using Diffusion Couples.” *Journal of the Less Common Metals* 37.1 (1974): 115-121. Print.

[38] Andersson, J.O. “A Thermodynamic Evaluation of the Fe-Mo-C System.” *Calphad* 12 (1988): 9-23. Print.

[39] Rawlings, R.D., and C.W.A. Newey. “Study of the Iron-Molybdenum System by Means of Diffusion Couples.” *Journal of the Iron and Steel Institute* 206 (1968): 723. Print.

[40] Okamoto, H. “Fe-Zr (Iron-Zirconium).” *Journal of Phase Equilibria*, 14.5 (1993): 652-653. Print.

[41] D. Arias and J.P. Abriata, In Massalski, T.B. *Binary Alloy Phase Diagrams.* 2nd ed. Materials Park: ASM International 2 (1988): 1798-1799. Print.

[42] Servant, C. “Experimental and Thermodynamic Assessment of the Fe-Zr System.” *Journal of Alloys and Compounds* 220.1-2 (1995): 19-26. Print.

[43] Granovsky, M.S., and D. Arias. “Intermetallic Phases in the Iron-rich Region of the Zr-Fe Phase Diagram.” *Journal of Nuclear Materials* 229 (1996): 29-35. Print.

[44] Jiang, M., K. Oikawa, T. Ikeshoji, L. Wulff, and K. Ishida. “Thermodynamic Calculations of Fe-Zr and Fe-Zr-C Systems.” *Journal of Phase Equilibria* 22.4 (2001): 406-417. Print.

[45] Stein, F., G. Sauthoff, and M. Palm. “Experimental Determination of Intermetallic Phases, Phase Equilibria, and Invariant Reaction Temperatures in the Fe-Zr System.” *Journal of Phase Equilibria* 23.6 (2002): 480-494. Print.

[46] Liu, Y., S.M. Allen, and J.D. Livingson. “An Investigation of Fe_3Zr Phase.” *Scripta Metallurgica Et Materialia* 32.8 (1995): 1129-1132. Print.

[47] Abraham, D.P., J.W. Richardson, and S.M. McDeavitt. “Formation of the $Fe_{23}Zr_6$ Phase in an Fe-Zr Alloy.” *Scripta Materialia* 37.2 (1997): 239-244. Print.

[48] Harda, H., S. Ishibe, R. Kanishi, and H. Sasakura. “Mossbauer Study of Fe-Zr Alloys Formed at Interfaces Between Fe and Zr Thin Films.” Japanese Journal of Applied Physics 25 (1986): 1842-1846. Print.

[49] Bhanumurthy, K., G. Kale, and S. Khera. “Reaction Diffusion in the Zirconium-Iron System.” *Journal of Nuclear Materials* 185.2 (1991): 208-213. Print.

[50] Domagala, R.F., D.J. McPherson, and M. Hansen. “Systems Zirconium-Molybdenum and Zirconium-Wolfram.” *Transactions of AIME* 197 (1953): 73-79. Print.

[51] Svechnikov, V.N., and A.C. Spektor. *Phase Transformation*. Kiev, Ukraine: Nauk Dumka, (1967): 123-128. Print.

[52] Rudy, E. “Ternary Phase Equilibria in Transition Metal-Boron-Carbon-Silicon Systems, Part V Compendium of Phase Diagram Data.” Technical Report AFML-TR-64-2, Air Force Materials Laboratory, Ohio (1969). Print.

[53] Samsonov, G.B., S.M Braun, and A.A. Rogozinskaya. *Izvestiya Vysshikh Uchebnykh Zavedenii Tsvetnaya Metallurgia* 15.6 (1972): 118-122.

[54] Miodownik, A.P. “The Effect of Magnetic Transformations on Phase Diagrams.” *Bulletin of Alloy Phase Diagrams* 2.4 (1982): 406-412. Print.

[55] Huang, K., Y. Park, A. Ewh, B.H. Sencer, J.R. Kennedy, K.R. Coffey, and Y.H. Sohn. “Interdiffusion and Reaction Between Uranium and Iron.” Journal of Nuclear Materials 424 (2012): 82-88. Print.

[56] LeClaire, A.D. *Diffusion in Body-Centered Cubic Metals.* Metal Park: Ohio, American Society for Metals (1965). Print.

[57] Murdock, J., T. Lundy, and E. Stansbury. “Diffusion of Ti44 and V48 in Titanium.” *Acta Metallurgica* 12.9 (1964): 103. Print.

[58] Peterson, N.L. “Self-diffusion in Pure Metals.” *Journal of Nuclear Materials* 69-70 (1978): 3-37. Print.

[59] Sanchez, J., and D. Defontaine. “Anomalous Diffusion in Omega Forming Systems.” *Acta Metallurgica* 26.7 (1978): 1083-1095. Print.

[60] Tiwari, G.P., and K. Hirano. “Interrelationship Between the Diffusion Behaviour and the Phase Transformation Characteristics.” Transaction of the Japan Institute of Metals 21.10 (1980): 667-673. Print.